Input-specific gating of NMDA amplification via HCN channels in mouse L2/3 pyramidal neurons

Viktor János Oláh[1], Jing Wu[2], Leonard K. Kaczmarek[2,3] & Matthew JM Rowan[1,4*]

[1]Department of Cell Biology, Emory University School of Medicine, Atlanta, GA, 30322, USA
[2]Department of Pharmacology, Yale University School of Medicine, New Haven, Connecticut 06520
[3]Department of Cellular and Molecular Physiology, Yale University School of Medicine
[4]Center for Neurodegenerative Disease, Emory University School of Medicine

***Address for Correspondence:**
Matt Rowan, PhD
Emory University School of Medicine
Department of Cell Biology
Atlanta, GA, 30322
Email: mjrowan@emory.edu

Citations: 72; *Figures*: 7 main figures; 6 supplementary figures

ABSTRACT

Layer 2/3 pyramidal cells (L2/3 PCs) play a crucial role in cortical information transfer. Although the dendritic arbors of L2/3 PCs are impressive, they often lack the distinct anatomical compartments characteristic of deeper L5 PCs. For example, many L2/3 PCs do not display an apparent distal tuft region. However, L2/3 PCs receive inputs from both thalamic (bottom-up) and cortical (top-down) inputs, which preferentially synapse onto their proximal and distal dendrites, respectively. Nonuniform organization of channels and NMDA receptors in L2/3 dendrites could serve to independently modulate these information streams to affect learning and behavior, yet whether L2/3 PC dendrites possess this capability has not been established. Here we found a previously unappreciated, non-uniform HCN channel distribution in L2/3 PCs, allowing for pathway-specific gating of NMDA receptor recruitment at bottom-up (proximal) but not top-down (distal) synapses. HCN availability shifted depending on developmental stage and neuromodulation, suggesting that the gain of thalamic and cortical-cortical signals in L2/3 may be independently modified *in vivo* across different timescales.

INTRODUCTION

Layer 2/3 pyramidal cells (L2/3 PCs) are the most numerous excitatory neurons in the neocortex. As a major component of the canonical circuit, L2/3 PCs are thought to play crucial roles in information transfer and gain control of cortical output(1). Thus, disambiguating the afferent circuit connections of L2/3 PCs has been a significant focus of neuroscience research in the past decade(2-5). However, understanding cellular mechanisms by which L2/3 PCs transform information is equally important (6-9). Like their more extensively studied counterparts (e.g., L5 PT-type PCs, hippocampal CA1 PCs), L2/3 PCs are equipped with an array of dendritic nonlinearities(10, 11), enabling complex subcellular computations. Nonetheless, L2/3 PCs exhibit marked disparities from other PC types as well. Their morphology is less segmented due to the lack of a distinctive apical tuft (except for the deepest layer 3 cells (12)). Their dendritic protrusions are also shorter and consequently possess less surface area over which specialized nonlinear operations may be actualized. Therefore, the applicability of currently established neuronal dynamics to L2/3 PCs is questionable.

Dendritic voltage-gated channels and receptors are crucial for diversifying the computational power of neuronal cells, by allowing for nonlinear processing of arriving synaptic inputs(13). Nonlinear processing is essential for proper brain function and has been implicated in critical tasks such as conscious perception(14-16) and processing of sensory and motor input(17). Therefore, a more comprehensive understanding of subcellular signal processing dynamics in L2/3 PCs is warranted. Dendritic hyperpolarization-activated nonselective cation (HCN) channels are a staple of several PC classes(18, 19), playing essential roles in regulating resting membrane potential, the normalization of synaptic events arriving at spatially mismatched locations, and establishing oscillation frequency-selectivity(16). Beyond exerting control over the general excitability of neurons, HCN channels contribute to synaptic plasticity, and can regulate working memory(16). HCN dysfunction can also contribute to epilepsy and pain(20). Electrophysiological detection of this current often relies on identification of a characteristic 'sag' potential, elicited by hyperpolarizing current injections. In L2/3 PCs, this sag potential is negligible in most cortical areas (but see (21)) thus HCN channels are often presumed to be missing from mouse L2/3 PCs (22). However, it has recently been proposed that HCN is a key determinant of L2/3 PC passive properties at membrane potentials close to rest, despite the lack of traditional HCN channel physiological markers (23). In contrast to mice, the presence of HCN channels in L2/3 PCs of primates and humans is unambiguously supported by functional and anatomical evidence as well (24, 25) (26).

Here we report that L2/3 PCs throughout the cortex express functionally relevant HCN channels with unexpected functions. We found that HCN channels robustly influence the overall

excitability of L2/3 PCs. Interestingly, we found that HCN channel availability in L2/3 PCs is biased in a unique proximal somato-dendritic manner, which is inverted with respect to L5 PT-type and hippocampal CA1 PCs (but see (27)), where HCN is enriched within their distal apical tufts(19, 28). In cooperation with local NMDA receptors, we found this L2/3 HCN organization could gate the amplification of proximal 'bottom-up' dendritic inputs, without affecting distal 'top-down' dendritic inputs. Furthermore, we found that HCN expression is robustly upregulated during early postnatal development, and that neuromodulation in adulthood can rapidly adjust HCN channel availability. Our results demonstrate that L2/3 PCs not only express dendritic HCN channels, but also employ these conductances in a previously unappreciated synaptic input-selective manner.

RESULTS

HCN channel expression in L2/3 PCs

HCN channels have been extensively documented and rigorously characterized in several cortical PC types(18), however, whether PCs residing in layer 2/3 of the mouse cortex express functionally relevant HCN channels remains ambiguous. Nonetheless, open-source snRNAseq (29) shows comparable HCN subunit mRNA levels in all cortical PC types of the visual cortex (Fig. 1a). Therefore, we investigated whether this mRNA signature translated to HCN surface expression. Immunohistochemical staining against HCN1 showed discernible somatic fluorescent signal in many cells residing in superficial layers of the cortex (Fig. 1b) along with staining of putative dendrites. To examine the potential functional role for HCN channels in L2/3 PCs, we performed *ex vivo* cell-attached recordings from visually identified L2/3 PCs in primary visual cortex slices from mature mice. Spike output upon extracellular stimulation (50 Hz) in layer 4 was then measured in control conditions and following pharmacological HCN channel block (Fig. 1c). We found that bath application of ZD-7288 (50 µM), a conventional blocker of HCN channels, significantly increased their firing (Fig. 1d,e). Similar results were obtained using another well-accepted HCN channel blocker; external Cs^+ (2 mM, Fig. 1f,g). This effect was unlikely due to presynaptic modulation of these synapses, as the paired-pulse ratio was unchanged in a set of separate whole-cell recordings coupled with stimulation in layer 4 (Fig. 1h). Together, these results indicate that L2/3 PCs express a functionally relevant set of HCN channels which can modulate AP firing following synaptic stimulation.

101 **HCN channels constrain the overall excitability of L2/3 PCs**

102 To investigate the role of HCN channels in regulating the excitability of L2/3 PCs, we performed
103 further L2/3 PC whole-cell recordings. A conventionally used assessment of HCN channel function is
104 the characterization of the sag potential(18). This hallmark of I_h activation is measured as the amount
105 of rectification detected in response to hyperpolarizing current injections. In line with previous
106 reports(30), we found that L2/3 PCs exhibited an unremarkable amount of sag potential at 'typical'
107 current commands. However, upon larger negative current injections, a discernable rectification was
108 revealed (Fig. 2a). In addition, the rectification of the steady-state responses was abolished in the
109 presence of external Cs^+, which could be restored by artificial I_h supplementation by dynamic clamp
110 (Fig. 2b). Similarly, sag became non-detectable when I_h was blocked, which could then be online
111 restored during recordings by dynamic clamp (Fig. 2c,d). Furthermore, we found that passive electrical
112 properties were also significantly modulated by HCN blockade (Fig. 2e,f, Supplementary Fig. 1),
113 however, action potential halfwidth was unaffected (1.04 ± 0.09 ms vs. 1.12 ± 0.17 ms for control vs.
114 CsMeSO4 bath application; p=0.324, t(6)=-1.073, Student's paired t-test; n=7. Together, these results
115 explain the dramatic effect of HCN blockade on L2/3 excitability (Fig. 1). The non-apparent sag
116 potential at conventional hyperpolarizing current steps is thus surprising, suggesting a markedly faster
117 occurrence of the I_h effect exists in L2/3 PCs which occludes the biphasic nature of the sag response.
118 To investigate this possibility, we measured the time constant of the immediate voltage responses. We
119 found a strong positive correlation between the amplitude of a passive current command and the
120 voltage response time constant, which was abolished by Cs^+ bath application (Fig. 2g). This confirms
121 that I_h has a strong effect during the initial phase of hyperpolarizing voltage responses, which may
122 contribute to the lack of detectable sag potential at modest current injections. However, other
123 biophysical mechanisms may also contribute to the muted sag effect in L2/3 PCs.

124 Next, we examined the voltage dependence and kinetic properties of I_h in L2/3 PCs in voltage
125 clamp (Fig. 2h). Significant Cs^+-sensitive (1mM) currents were activated at subthreshold membrane
126 potentials, with half-activation voltages more negative than the resting membrane potential, and with
127 relatively fast activation kinetics (Fig. 2i,j). Overall the pharmacological profile, effects on passive
128 electrical properties, and voltage dependence all point to previously published data describing HCN
129 channels (31). Together these results indicate that L2/3 PCs express a functionally relevant population
130 of HCN channels, which constrain the excitability of these cells. Similar responses were observed in
131 voltage clamp recordings across several cortical regions (e.g., in S1, M1, and A1; Supplementary Fig.
132 2), suggesting that HCN channels are a consistent feature in L2/3 PCs.

133 **Noncanonical subthreshold signal processing in L2/3 PCs by I_h**

134 Electrical signals at different dendritic compartments undergo distance-dependent distortion (28, 32),
135 which has a major effect on neuronal function in cells with extensive dendritic branching (33). To
136 counteract these effects, larger L5 PT-type PCs and CA1 PCs express HCN channels with nonuniform
137 distributions (19, 31). As L2/3 PCs have a much more compact morphology, synaptic input distortions
138 might be less severe, raising the possibility of an alternative function of HCN channels in these cells.
139 Thus, to investigate the distance-dependence of HCN on L2/3 synaptic inputs, we made whole-cell
140 patch recordings from Alexa-594 filled L2/3 PCs and performed extracellular minimal stimulation at
141 different dendritic locations guided with 2P microscopy (Fig. 3a). Elicited EPSPs likely reflect the
142 activation of a single axon, as stimulus intensity was set to achieve an ~50% failure rate(34). As HCN
143 deactivation has been shown to strongly impact the duration of synaptic events(28, 32), we quantified
144 changes in the half-width of locally evoked EPSPs, here using the HCN-selective blocker ZD-7288
145 (50 μM). Surprisingly, our results were in contrast to previous reports in L5 PT-type and CA1 PCs, in
146 that I_h block had a far smaller effect on the time-course of distally-evoked (>100 μm distance from the
147 soma) synaptic responses. In contrast, proximal inputs (<100 μm) were markedly more broadened after
148 I_h blockade (Fig. 3b,c). These results suggest that L2/3 PCs are equipped with a distinctive subcellular
149 HCN distribution, potentially contributing to noncanonical distance-dependent input amplification
150 along the dendritic axis of L2/3 cells.

151

152 **Pathway-specific modulation of synaptic information**

153 L2/3 PCs receive information from distinct brain regions, such as "top-down" (cortical-cortical) axons,
154 generally arriving to layer 1(35) and "bottom-up" (thalamocortical/layer 4) axons, terminating on
155 proximal dendrites located in layer 4 and 2/3 (36). Due to the stronger proximal effect of HCN on L2/3
156 PC EPSPs, we explored whether this modulation yielded input-pathway-specific differences. Whole-
157 cell recordings were again obtained from L2/3 PCs, and EPSPs were elicited by minimal stimulation
158 with electrodes situated to preferentially stimulate either layer 4 or layer 1 axons (electrode placement
159 ~200μm laterally from recorded PC in either layer). Inhibition was left intact in these experiments.
160 While most evoked EPSPs were small (< 0.5 mV), a subset evoked with minimal stimulation was
161 outsized (we deemed these here as L4-Type I and L4-Type II inputs, respectively; Fig. 3d,
162 Supplementary Figure 3). The L4-Type II events were substantially larger than previous reports(3) but
163 see (37).

164 I_h blockade significantly broadened elicited EPSPs when the stimulation electrode was placed
165 in layer 4, but not in layer 1 (Fig. 3e). Consequently, the effect of Cs^+ on the EPSP integral was
166 significant for L4 inputs, but not L1 inputs (Fig. 3f). The effect of Cs^+ on EPSP half-width and voltage
167 integral was similar for both L4-Type I and L4-Type II inputs, suggesting intermingled termination
168 zones(36) in proximal dendrites. HCN channels are notable for their ability to restrain temporal
169 integration of synaptic inputs(28). Therefore, we repeated these experiments using more high-
170 frequency stimulation (5 stimuli at 50 Hz; Fig. 3g; inhibition was blocked due to strong inhibitory
171 recruitment at 50Hz). In accordance with the effect on single EPSPs, summation of L1 (i.e., distal)
172 inputs was unaltered with HCN block. In contrast, HCN blockade led to increased temporal summation
173 of L4-Type I inputs (Fig. 3h,i). Summation of L4-Type II inputs was not affected by HCN channel
174 block, suggesting further diversification between L4-Type I and L4-Type II inputs as well.
175 To more accurately evaluate whether synaptic signaling from *bone fide* bottom-up and top-
176 down axons are differentially regulated by HCN, we next injected a CaMKII-driven, C1V1-expressing
177 AAV into either the LGN or the lateromedial visual (LM) areas in separate experiments (LM, Fig.
178 3j,k). LGN and LM-originating axons are thought to preferentially synapse onto proximal and distal
179 L2/3 dendrites, respectively (38-41). In these experiments, short LED-directed amber light pulses
180 could reliably elicit EPSPs in L2/3 PCs (Fig. 3k). We used a 'minimal' opto stim approach for these
181 experiments, meaning we used as low light power as possible to reliability (1 ms pulses at 0.2 Hz)
182 evoke EPSPs, while avoiding AP firing and thus further network recruitment. Inhibition was not
183 blocked during optical stimulation. These optogenetic experiments revealed a negligible effect of Cs^+
184 on top-down, LM-driven EPSPs. Conversely EPSPs were significantly broadened following Cs^{2+} of
185 bottom-up, LGN-originating EPSPs (Fig. 3k,l). Together these results suggest that HCN channels
186 preferentially regulate thalamic-originating, bottom-up nonlinear signaling in proximal dendritic
187 regions of L2/3 PCs.
188

189 **I_h channels constrain NMDA receptor-dependent synaptic boosting in proximal dendrites**

190 In a passive environment, dendritic filtering(42) creates attenuated (i.e., wider) EPSPs when
191 originating further from the soma. Yet our results show an opposite phenomenon with HCN channels
192 blocked. It has been described that reduced HCN availability can facilitate dendritic boosting
193 mechanisms via activation of either voltage-gated(43) or NMDA(44) channels. To investigate possible
194 contributions of dendritic voltage-dependent processes, we next performed NEURON computational
195 simulations using a realistic L2/3 PC dendritic morphology(45). Inserting voltage-gated sodium or

196 potassium channels with various distributions could not recapitulate our distance-dependent EPSP
197 observations (Supplementary Figure 4.). Thus, we next investigated whether NMDA receptors might
198 play a role in the observed phenomenon due to their described overwhelming contribution to *in vivo*
199 activity in L2/3 PCs (8, 46).

200 We first tested whether NMDA receptors contribute to spontaneously occurring synaptic inputs
201 (sEPSPs) in L2/3 PCs(47) in slice experiments. Due to potential alterations in spontaneous release and
202 overall circuit activity, extracellularly applied NMDA blockers may introduce significant confounds
203 for this line of investigation especially as spontaneous synaptic potentials show tremendous variability
204 in frequency, amplitude, and kinetics. To overcome this conundrum, we designed a custom-built
205 pipette attachment through which the intracellular solution could be stably exchanged during whole-
206 cell recordings (48). We recorded sEPSPs in L2/3 PCs first using control intracellular solution, which
207 was then exchanged to a 50 μM MK-801 (non-competitive NMDA receptor antagonist) containing
208 intracellular solution (Fig. 4a). To also capitalize on the voltage-sensitivity of NMDA receptors,
209 average peak amplitudes were recorded at two different membrane potentials for each intracellular
210 condition; -80 mV and -55 mV (resting membrane potential, and a somatic membrane potential
211 depolarized enough to partially unblock NMDA receptors (49)). Due to the small nature of L2/3 PC
212 sEPSPs, quantification of other waveform parameters (i.e., EPSP width) was avoided. After
213 quantifying the mean sEPSP peak at -80 mV, we calculated the expected (linear) sEPSP peak at -55
214 mV and compared this prediction to our observations of -55 mV. We found that sEPSPs were
215 significantly larger than predicted after depolarization (Fig. 4b), alluding to the presence of a nonlinear
216 subthreshold amplifying mechanism. We found that intracellular MK-801 solution exchange could
217 severely dampen this synaptic amplification (Fig. 4c), indicating that NMDA receptors actively
218 contribute to shaping naturally occurring sEPSPs in L2/3 PCs. The effect of pipette perfusion itself on
219 our measurements was negligible (Supplementary Fig. 5)

220 Having established that NMDA receptors play an active role in modulating sEPSPs, we next
221 utilized computational simulations to explore whether non-uniform NMDA recruitment could explain
222 the subthreshold boosting in proximal L2/3 synapses, as described earlier following HCN channel
223 blockade (Fig. 3b). Accordingly, this initial model did not include HCN channels. NMDA was inserted
224 into a NEURON model with varying distributions and conductance densities (Fig 4d) to systematically
225 evaluate a large parameter space. These simulations (Fig. 4e) revealed that a proximally-biased NMDA
226 distribution (50) could indeed produce local EPSP boosting (Fig. 4e,f) similar to our experimental
227 findings in an HCN-lacking condition.

228 Because HCN channels can reduce NMDA recruitment during synaptic signaling, we next
229 explored whether proximal enrichment of HCN allows for bottom-up-specific gating of NMDA
230 amplification (Fig. 4e,f) now using complimentary slice experiments. To accomplish this, we recorded
231 L2/3 EPSPs originating from both proximal L4 and distal L1 inputs during each recording (i.e., two
232 stimulation locations for each cell; Fig. 4g). For each recording, one pharmacological condition was
233 evaluated to sequentially explore the interplay between HCN and NMDA (Fig. 4g). In control
234 conditions, L4-evoked EPSPs were slightly narrower than L1-evoked EPSPs. This layer-specific
235 relationship was inverted following extracellular Cs^+ to block HCN (Fig. 4g,h). This result
236 recapitulated our NEURON simulation best-fit prediction, where a proximally-biased NMDA
237 distribution was necessary (Fig. 4f).

238 To confirm that this L4-specific EPSP broadening after HCN channel block was indeed due to
239 NMDA-inducted boosting, as predicted in our simulations (Fig. 4f), we next examined L4 and L1-
240 evoked EPSPs using Cs^+ and intracellular MK-801. In the presence of internal MK-801, the broadening
241 effect of Cs^+ on L4-evoked EPSPs was abolished, thereby reverting the L4-L1 EPSP relationship to a
242 control-like state. (Fig. 4g,h). The NMDA receptor contribution is unlikely related to different event
243 amplitudes in proximal and distal sources, as the peak and halfwidth of the elicited EPSPs in our dataset
244 showed no correlation (Supplementary Fig. 6). Together, our modeling and experimental results
245 indicate that NMDA-directed amplification of L4 inputs is strongly constrained by a proximal HCN
246 bias in L2/3 PCs dendrites, allowing for pathway-specific modulation of 'bottom-up' inputs without
247 affecting those arriving from 'top-down' L1 axons.

248

249 **Noncanonical HCN distribution predicted in L2/3 PCs**

250 We next carried out a more complete computational simulation which included both HCN and NMDA
251 in a L2/3 PC. To test whether our results could be explained due to a non-uniform HCN distribution,
252 HCN channels were inserted into the model with varying distributions and conductance densities (Fig
253 5a) to evaluate a large parameter space. Our simulations revealed that proximal bias in HCN channel
254 distributions could best recapitulate our observations of proximally and distally originating EPSP
255 waveforms in control conditions (Fig. 5b,c). This is in line with the proximal HCN1 channel staining
256 (Fig. 1) revealed by immunohistochemistry. Together our results indicate that L2/3 PCs have a
257 proximal HCN channel bias, whereas previous studies found a distal dendritic HCN bias in L5 PT-type
258 PCs and CA1 PCs(19, 31), which could constrain NMDA receptor amplification in an input-specific
259 manner.

260 **Tight developmental upregulation of Layer 2/3 HCN channels**

261 Due to the ability of HCN channels to regulate NMDA boosting shown earlier, modifying HCN
262 availability or expression may represent an important activity or plasticity gate in L2/3. Previously we
263 found that HCN recruitment was upregulated in interneurons during early development(51). Indeed,
264 several ion channels show postnatal maturation in their biophysical properties and surface
265 expression(52), raising the possibility of a different proximo-distal HCN bias in young L2/3 PCs
266 compared to adult animals. To examine this possibility, L2/3 PCs were recorded at three developmental
267 time points (1st, 2nd and 6th postnatal week) in S1 cortex. Our assessment showed that a rapid
268 developmental HCN upregulation occurs between 1 and 2 weeks old. We also found that 1 week old
269 L2/3 PCs displayed markedly different passive properties, while 2-week-old cells were quite similar
270 to mature cells (Fig. 6a). The non-quantifiable sag potential in 1 week old animals implies the lack of
271 I_h current at this developmental time point, however, the disproportionately large input resistance and
272 elevated resting membrane potential also suggests that other background leak channels may also be
273 missing at this developmental window (Fig. 6b). Subsequent voltage clamp recordings confirmed that
274 in 1 week old animals, L2/3 PCs do not possess a considerable amount of I_h in contrast to 2 and 6 week
275 old animals (Fig. 6c,d). We found that both the resting membrane potential and peak I_h conductance
276 changes throughout development were tightly (negatively) correlated (Fig. 6e). This provides
277 additional evidence for parallel maturation of HCN with other leaky channels, as HCN channel
278 expression alone would be predicted to shift the membrane to more depolarized potentials (Fig. 2e).

279 Next, we mapped the distance-dependence dendritic EPSP kinetics in 1 week old animals (Fig.
280 6f). We found a surprising 'non-Rallian' negative correlation between EPSP halfwidth and stimulation
281 distance from the soma (Fig. 6g, h), similar to our previous results from mature neurons with HCN
282 channels blocked (Fig. 3a,b). This suggests the presence of nonlinear boosting mechanisms (e.g.,
283 NMDA) in proximal dendrites of developing L2/3 PCs, similar to mature cells, but which are unabated
284 due to the lack of HCN at this early developmental stage.

285

286 **I_h dependent neuromodulation of L2/3 PC activity by serotonergic inputs**

287 Whether the mature brain possesses mechanisms to modulate HCN in L2/3 PCs is unknown.
288 Nonetheless, previous work in cortical L5 PT-type PCs shows that I_h currents can be modulated
289 following 5-HT_7 serotonergic receptor activation(53). L2/3 PCs are extensively innervated by
290 serotonergic axons from the dorsal raphe (54), providing a potential framework to modify HCN
291 availability. Single-cell RNA-seq (29) showed that L2/3 PCs do express 5-HT_7 receptors, interestingly,

292 at higher levels than all other cortical PCs (Fig. 7a). We pharmacologically evaluated a potential role
293 of serotonergic HCN regulation by bath application of 5-carboxamidotryptamine (5-CT; 30 nM), a
294 specific 5-HT_7 agonist. 5-CT application significantly reduced evoked firing of L2/3 PCs during
295 extracellular stimulation in L4 (Fig. 7b). Current clamp experiments revealed that the rectification of
296 steady-state voltage responses to hyperpolarizing current injection was amplified with 5-CT (Fig. 7c),
297 likely due to the increased availability of HCN channels due to a rightward shift in their activation
298 voltage-dependence (Fig. 7d). 5-CT also reduced L2/3 input resistance potentially via HCN regulation,
299 however, did not yield a depolarizing effect on the resting membrane potential nor affect AP threshold
300 (Fig. 7e). Importantly, 5-CT had no impact on the firing responses of L2/3 PCs when I_h currents were
301 blocked with background Cs^+ throughout the experiment (Fig. 7f). Furthermore, the dampening of
302 neuronal output was not related to an downregulating effect of 5-HT7 on NMDA receptors (Fig. 7g,
303 (55)). Together these results indicate that neuromodulation represents an endogenous mechanism by
304 which HCN availability can be altered in L2/3 PCs. Further studies on the input-specific effects of
305 neuromodulation on dendritic nonlinearities in L2/3 PCs should thus be considered.
306
307 **DISCUSSION**
308
309 Precise communication between cortical neurons relies on discrete pre- and postsynaptic forms of
310 information transfer at synapses. The majority of cortical synapses terminate along the dendritic tree
311 (56) where, based on local active and passive electrical properties, various types of nonlinear
312 transformations occur. The spatially and electrically disjointed nature of dendrites (57) from the rest
313 of the cell allows for local, soma-independent computation. For example, perturbing active dendritic
314 elements (i.e., local conductances) can impair several fundamental cortical circuit tasks (36) such as
315 perception (14), underlining the necessity for compartmentalized information processing. Further,
316 single-subunit model simulations are unable to reproduce *in vivo* observed activity patterns of L2/3
317 PCs(9). Here, by combining *ex vivo* current clamp, synaptic stimulation, and ion channel recordings
318 with empirically informed, biophysically realistic simulations, we demonstrate that L2/3 PCs in
319 sensory cortex express a previously unappreciated, proximally-biased HCN channel distribution. Due
320 to an apparent universal HCN expression in L2/3 cells from each cortical region, this arrangement
321 should allow for modification of synaptic gain across all primary sensory areas of cortex. One of the
322 basic functions of L2/3 PCs in sensory cortex is to encode first-order information, such as the
323 orientation of visual input(2, 58, 59). Several investigations propose that arithmetic summation of a
324 number of similarly tuned synapses will dictate whether these neurons will fire in response to sensory

input (60). However, numerous dendritic nonlinearities have been established in L2/3 PCs, such as NMDA receptors (8), sodium channels (11), and calcium channels (10, 61), which also contribute to this process. Here we demonstrate that L2/3 PCs express a functionally relevant population of HCN channels well situated to modify the gain of cortical sensory and contextual information processing.

We report that HCN channels in L2/3 constrain fundamental aspects of cellular excitability, such as input resistance and resting membrane potential. This is likely due to a strong proximal somato-dendritic distribution of HCN channels, as observed in immunohistochemical experiments here. Likely due to their influence on input resistance, HCN blockade resulted in greatly increased AP firing during extracellular stimulation. L2/3 HCN channels strongly dampened excitatory synaptic inputs, however, only to those arriving at proximal dendritic locations. In line with this result, HCN channels reduced the timecourse of synaptic inputs following local stimulation in L4, but left those following L1 stimulation unaffected. Together with additional input-specific pharmacological experiments, NEURON simulations demonstrated that this input-specific synaptic phenomenon could indeed be explained by a proximal HCN channel distribution in dendrites putatively situated in L4 and L2/3. This was apparently only possible with a concurrent proximal NMDA recruitment bias. This predicted global organization should not be confused with observed differences in NMDA recruitment along the axis of individual L2/3 basal dendrites (47). Our predictions of NMDA distributions require further evaluation at the spine-synapse level. Although a proximal-basal dendrite NMDA receptor distribution is in line with findings from L5 PT-type PCs (62), HCN channels are instead enriched distal dendritic compartments in these PC types (19, 31). Thus the unique proximal HCN recruitment in L2/3 PCs permits pathway-specific control of synaptic amplification, as bottom-up (i.e., L4 originating) inputs target proximal dendritic compartments homogeneously (36). This was in opposition to top-down inputs, whose axons largely target distal dendrites in L2/3 PCs (63), as these synapses were unaffected by HCN channel blockade. To fully understand how compartment-specific pathways are functionally regulated, further anatomical and *in vivo* imaging experiments are needed to establish the distribution and synaptic dynamics of L4 and L1 inputs along the L2/3 PC dendritic tree.

HCN channels appear well suited to regulate the synaptic and intrinsic properties of L2/3 PCs, for example, if their availability is plastic or developmentally regulated. Previously, we found that HCN channel availability was upregulated in GABAergic interneurons during development, resulting in reduced propagation of subthreshold signals in mature axons (51). Interestingly, we found that L2/3 PCs in young animals (1 week old) lacked HCN currents. Together, these results suggest a universal developmental HCN upregulation across neuron types. In L2/3 PCs, the HCN channel maturation window was rapid and almost complete by the second postnatal week. Therefore critical period

358 plasticity (64) and developmental I_h upregulation occur during a similar developmental window,
359 suggesting a causal relationship. In addition to the robust developmental regulation of HCN channels,
360 we also found that modification of HCN channel availability was also possible in the adult cortex,
361 following serotonergic (5-HT_7) receptor-mediated biophysical regulation. This was likely due to a
362 metabotropic process that increases cytosolic cAMP levels by stimulating adenylate cyclase(65) which
363 in turn modulates HCN channel properties. This raises the intriguing possibility that neuromodulation
364 could induce nonstationary conditions in mature L2/3 circuits, for example, in re-biasing of bottom-up
365 vs. top-down information, experience-dependent plasticity (66), or even for reopening of critical
366 window-like states (67). A recent finding demonstrated increased spine density and stability during
367 early development due to enhanced 5-HT release in L2/3 PCs of the prefrontal cortex(68), which
368 suggests that serotonin is responsible for not only the morphological, but the physiological regulation
369 of L2/3 PC spines as well.

370 As L2/3 PCs are one of the most abundant cell populations of the neocortex, HCN channels in
371 these cells may exert overwhelming control over cortical excitability and thus cognition and memory.
372 Cell non-autonomous HCN channel dysregulation manifests in clear behavioral changes, such as
373 altered spatial learning (69) or impaired working memory (70). Curiously, higher HCN1 protein levels
374 in the postmortem brain also correlate with cognitive resilience in aging humans (71). Therapeutic
375 HCN channel modulation aimed at restoring healthy brain function in distinct pathophysiological states
376 has consequently garnered significant interest (72-74), as both HCN1 and HCN2 are linked to
377 neuropathic pain (75) and for treating major depressive disorder (73, 74, 76). Here we demonstrate that
378 activation of the serotonergic receptor 5-HT_7 alters HCN channel function in L2/3 PCs, resulting in
379 reduced PC excitability, similar to L5 PT-type PCs (53). 5-HT_7 receptor targeting agents are highly
380 effective psychopharmacological compounds. Agents such as the antidepressant *vortioxetine* has a
381 relevant therapeutic concentration that functionally suppresses 5-HT_7 (77), and the mood-stabilizing
382 antipsychotic agent *lurasidone* possesses an even higher binding affinity to 5-HT_7 (78). Commonly
383 used anesthetic drugs also modulate HCN channel action (79, 80), implying the need to investigate
384 anesthesia-related mechanisms and confounds in L2/3 in both therapeutic and experimental settings.
385 Together, we argue that HCN channels are present and functionally relevant in L2/3 PCs. As L2/3 PCs
386 are one of the largest cell populations in the brain, and as HCN channels are the target of several current
387 therapeutics, future research should consider their role in these cells in basic and clinical studies.
388
389
390

391 **METHODS**

392

393 **Acute slice preparation**

394 All animal procedures were approved by the Emory University IACUC. Acute slices from cortex were
395 prepared from mature C57Bl/6J mice (6–10 weeks old). Male and female mice were used for all
396 experiments with data collected from ≥3 mice per experimental condition. Mice were first anesthetized
397 with isoflurane and perfused with ice-cold cutting solution (in mM) 87 NaCl, 25 $NaHO_3$, 2.5 KCl, 1.25
398 NaH_2PO_4, 2 $MgCl_2$, 1 $CaCl_2$, 10 glucose, and 75 sucrose. Thereafter, mice were terminated by
399 decapitation and the brain immediately removed by dissection. Brain slices (250 µm) were sectioned
400 in the coronal plane using a vibrating blade microtome (VT1200S, Leica Biosystems) in the same
401 solution. Slices were collected from V1 and from S1, M1 and A1 for a subset of experiments. Slices
402 were transferred to an incubation chamber and maintained at 34°C for ~30 min and then at 23–24°C
403 thereafter. During whole-cell recordings, slices were continuously perfused with (in mM) 128 NaCl,
404 26.2 $NaHCO_3$, 2.5 KCl, 1 NaH_2PO_4, 1.5 $CaCl_2$, 1.5$MgCl_2$, and 11 glucose, maintained at 30.0°C ±
405 0.5°C. All solutions were equilibrated and maintained with carbogen gas (95% O_2/5% CO_2)
406 throughout.

407 **Intracranial viral injections:**

408 5-8 week old mice were injected with AAV.CAMKII.C1V1/eYFP (0.2 µl total) in the lateromedial
409 visual area (LM) or the lateral geniculate nucleus (LGN). During intracranial injections mice were
410 head-fixed in a stereotactic platform (David Kopf Instruments) using ear bars, while under isoflurane
411 anesthesia (1.5-2.0%). Thermoregulation was provided by a heating plate using a rectal thermocouple
412 for biofeedback, thus maintaining core body temperature near 37°C. Bupivacaine was subcutaneously
413 injected into the scalp to induce local anesthesia. A small incision was opened 5-10 minutes thereafter
414 and a craniotomy was cut in the skull (< 0.5 µm in diameter) to allow access for the glass microinjection
415 pipette. Coordinates (in mm from Bregma) for microinjection in the LM were X = ± 3.5; Y = -3.87; α
416 = 45°; Z = 0.7, coordinates for the LGN were X = ± 2.0, Y = -2.0; α = 0°; Z = -2.45. Viral solution
417 (titer 1 x 10^{13} vg/mL) was injected slowly (~0.02 µL min-1) by using a Picospritzer (0.2 µL total).
418 After ejection of virus, the micropipette was held in place (5 min) before withdrawal. The scalp was
419 closed with surgical sutures and Vetbond (3M) tissue adhesive and the animal was allowed to recover

420 under analgesia provided by injection of carprofen and buprenorphine SR. After allowing for onset of
421 expression, animals were sacrificed acute slices were harvested.

422 **Electrophysiology**

423 L2/3 PCs were targeted for somatic whole-cell recording in the layer 2/3 region of primary visual
424 cortex by gradient-contrast video microscopy. Electrophysiological recordings were obtained using
425 Multiclamp 700B amplifiers (Molecular Devices). Signals were filtered at 6–10 kHz and sampled at
426 50 kHz with the Digidata 1440B digitizer (Molecular Devices). For whole-cell recordings, borosilicate
427 patch pipettes (2.5-3.5 MΩ tip resistance) were filled with an intracellular solution containing (in mM)
428 124 potassium gluconate, 2 KCl, 9 HEPES, 4 $MgCl_2$, 4 NaATP, 3 l-ascorbic acid, and 0.5 NaGTP.
429 Pipette capacitance was neutralized in all recordings and electrode series resistance was compensated
430 using bridge balance in current clamp. Liquid junction potentials were uncorrected.

431 For cell attached recordings seal resistance of >1GΩ was established, for accurate measurement of
432 action potentials. Cells were held at -80 mV. A stimulating electrode (2.5-3.5 MΩ tip resistance, filled
433 with extracellular solution) was placed in either layer 4 or layer 1 region of the visual cortex, at least
434 200 µm away from the recorded soma. Stimulation intensities were calibrated to reliably elicit at least
435 3, but no more than 10 action potentials during the 20 consequent stimuli (50 Hz, 30 s inter-trace
436 intervals, 10-50 µs stimulus length). Stability of the elicited responses was confirmed by an initial 15
437 repeated measurements. Recordings were post hoc filtered at 2 kHz to remove stimulation artifacts.

438 Recordings had a series resistance <20 MΩ. Membrane potentials were maintained near –80 mV during
439 current-clamp recordings using constant current bias. AP trains were initiated by somatic current
440 injection (300 ms) normalized to the cellular capacitance in each recording measured immediately in
441 voltage clamp after breakthrough (81). Cellular electrical and firing parameters were established by
442 recording voltage responses to current steps between -6 pA/pF and 20 pA/pF. Sag potential was
443 measured at the -6 pA/pF step, by comparing the negative peak within the first 100 ms of the
444 hyperpolarized voltage response and the mean voltage during the last 50 ms of the stimuli. Input
445 resistance was measured by averaging voltage responses to a 20 pA prepulse current step. Sag ratio
446 was determined as the ratio between the sag amplitude and the steady-state response at the -6 pA/pF
447 current step, except when cells were recorded for measuring neuromodulation (Fig 7.), as those
448 experiments were significantly more time-consuming. In these cases, -2 pA/pF current injection was
449 provided.

450 To establish distance dependent EPSP kinetics, cells were filled with 10 μM Alexa-594. Dendrites
451 were visualized after cell fill with Alexa 594 (10μM) with two-photon laser scanning microscopy using
452 a commercial scan head (Ultima; Bruker Corp) fitted with galvanometer mirrors using a 60x, 1.0 NA
453 objective. The fluorophore was allowed to equilibrate for at least 10 minutes before imaging. The
454 stimulating electrode, filled with extracellular recording solution, was placed in close proximity (<5
455 μm) of the two-photon visualized dendrite. Stimulation intensity was calibrated to elicit an EPSP with
456 <1 ms delay and approximately 50% failure rate (54.21 ± 8.72%, n= 41). The 50% failure rate was
457 necessary in order to maximize the possibility of stimulating a single input. For L1, L4-Type I, and
458 L4-Type II input stimulations the procedure was the same. Synaptic summation was probed by eliciting
459 5 consequent responses at 50 Hz. Stimulation intensity was elevated during these recordings to elicit
460 synaptic responses every time for the first stimuli as failures introduced by lower stimulation intensities
461 can yield inconsistent input activation during the 5 stimuli. Inhibitory blocker SR95531 (10 μM) was
462 only included during signal summation (50 Hz stim) experiments, as our intention was to examine
463 single inputs in an intact system. However, repeated stimuli recruited significant inhibitory components
464 as well, therefore the use of inhibitory blockers was warranted for the uncontaminated analyses of our
465 recordings for the 50Hz repetitive stimulation experiments. Z-stacks were created from the stimulated
466 dendritic region and the connected soma as well for 3D reconstruction in order to establish exact
467 dendritic distances. The group of distal dendritic branches only included a fraction of apical dendrites,
468 however proximal dendrites included both a fraction of apical and basal dendrites, for two reasons;
469 first, basal dendrites are significantly shorter than apical dendrites and our recordings did not include
470 any basal dendrites extending beyond 200 μm, and second, in superficial L2 pyramidal cells classifying
471 dendrites that extend radially into apical or basal classes in ambiguous.

472 For voltage-clamp recordings, cells were patched in normal extracellular solution to first record their
473 firing patterns. Voltage protocols for I_h current measurements consisted of 300 or 500 ms long voltage
474 steps between −150 and −60 mV. Activation time constant was measured by fitting the initial 100 ms
475 of the current response with a single exponential function. In a subset of recordings CsMeSO4 (2 mM)
476 was bath applied after recording control current responses, to establish cesium-sensitive I_h current
477 kinetics and voltage dependence by subtraction. Series resistances were between 6–20 MΩ (75–80%
478 compensated with 53 μs lag) and were constantly monitored. Data were discarded if the series
479 resistance changed more than 25%.

480 The dynamic clamp system was built in-house based on a previous publication(82), related online
481 available materials available here: (http://www.dynamicclamp.com/). The equations governing the
482 implemented gHCN were identical to those used in the NEURON model construction. Synaptic
483 conductances were built-in predefined conductances available from http://www.dynamicclamp.com/.

484 **Intracellular solution perfusion**

485 Intracellular solution was perfused by a custom-built tubing and relay system attached to the pipette
486 holder. Briefly, the pipette was filled with normal intracellular solutions to measure firing patterns and
487 subsequent control measurements of spontaneous and elicited EPSPs. Next, a second intracellular
488 solution was introduced to the pipette through a small tube drilled through the pipette holder, by
489 applying miniscule positive pressure. The intracellular fluid levels were marked before the recording
490 and through a second tube the intracellular solution was siphoned out, to not alter established pipette
491 capacitance. During initial trial experiments using fluorophores in the second intracellular solution it
492 was determined that two minutes is enough for complete exchange of the intracellular solution and
493 intracellular equilibration as well. Data were discarded if the series resistance or pipette capacitance
494 changed more than 20%.

495 **Immunohistochemistry**

496 Two-month-old mice were anesthetized with Nembutal (50mg/mL, i.p.) and perfused transcardially
497 with 4% paraformaldehyde (PFA), 0.05% glutaraldehyde in phosphate buffered saline (PBS). After
498 perfusion, brains were removed from the skull and immersed in 4% PFA overnight at 4°C. Coronal
499 100 µm-thick sections were then cut on a Vibratome (Leica V1000). Brain slices were permeabilized
500 and incubated in blocking buffer for one hour at room temperature. After blocking, sections were
501 overlaid with primary antibody to HCN1 (1:200, Thermo Fisher Scientific) overnight at 4 °C, then
502 subjected to a 1 h incubation with secondary antibody (Goat anti-Rabbit IgG, 1:200, Thermo Fisher
503 Scientific) at room temperature. Stained sections were mounted with DAPI-containing mounting
504 solution and sealed with glass coverslips. Confocal imaging was carried out on a Leica SP5 MP.

505 **NEURON modeling**

506 Computer simulations were performed using the NEURON simulation environment (versions 7.5 and
507 7.6, downloaded from http://neuron.yale.edu). A constrained NEURON model with an active somatic

508 compartment was downloaded from the publicly available Cell Type Database of the Allen Institute
509 (http://celltypes.brain-map.org/experiment/electrophysiology/487661754). Passive properties (axial
510 resistance, specific membrane capacitance and leak conductance density) were altered manually to
511 recreate passive membrane potential responses of whole-cell recorded L2/3 PCs for given stimulus
512 intensities. Both transient and persistent potassium channels were taken out of the model to gain
513 simulation speed as the aim of the simulations was to reproduce subthreshold EPSP dynamics. Final
514 simulations were rerun with intact sodium currents as well to confirm the lack of alterations introduced
515 by these channels. The I_h conductance was based on the built-in Hodgkin–Huxley model of NEURON
516 with freely adjustable sets of parameters(83). I_h model parameters were constrained by our whole-cell
517 voltage clamp recordings. The steady-state activation was governed by the following equation:

518 $$minf = \frac{1}{1 + e^{\frac{v+21.945}{6.85}}}$$

519 where v is the local membrane potential. Due to the lack of apparent inactivation, the model operated
520 with a single gate (activation).

521 The activation and deactivation time constant was defined as

522 $$mtau = 25.46 * e^{-0.5*\left(\frac{v+100.28}{16.2}\right)^2}$$

523 To simulate EPSP kinetics, a movable spine (length: 0.6 µm, diameter: 0.6 µm, axial resistance: 150
524 Ωcm), with spine neck (length: 2 µm, diameter: 0.1 µm, axial resistance: 100 Ωcm) was created. Leak
525 conductance was inserted into both compartments, along with the fitted conductance model. Synaptic
526 inputs were supplemented by using NEURON's built-in AlphaSynapse class. To probe the contribution
527 of specific dendritic conductances to shaping the distance-EPSP halfwidth relationship, selected
528 conductance models were inserted into both apical and basal dendrites with a Gaussian distribution.
529 This curve was selected as modulation of the Gaussian curve's width and y-offset can reproduce a wide
530 variety of feasible distributions such as linear, exponential, or hot-zone-like expression. To model the
531 contribution of dendritic sodium, potassium, and calcium channels to input modulation, NaTs, Kv3_1
532 and Ca_LVA models were selected. Distribution approximation was done by grid search to avoid local
533 fitting minimums. NMDA receptors were implemented based on a previous publication (84). During
534 the fitting procedure, NMDA activation voltage and AMPA:NMDA ratios were adjusted by a grid
535 search algorithm.

536 **Statistics**

537 Averages of multiple measurements are presented as mean ± SD. Data were statistically analyzed by
538 ANOVA test using Origin software and custom-written Python scripts. Normality of the data was
539 analyzed with Shapira-Wilks test.

540

541 **Data and software availability**

542 All code used for simulating single and multicompartmental NEURON models will be made available
543 on GitHub and public repositories upon VOR.

544

545

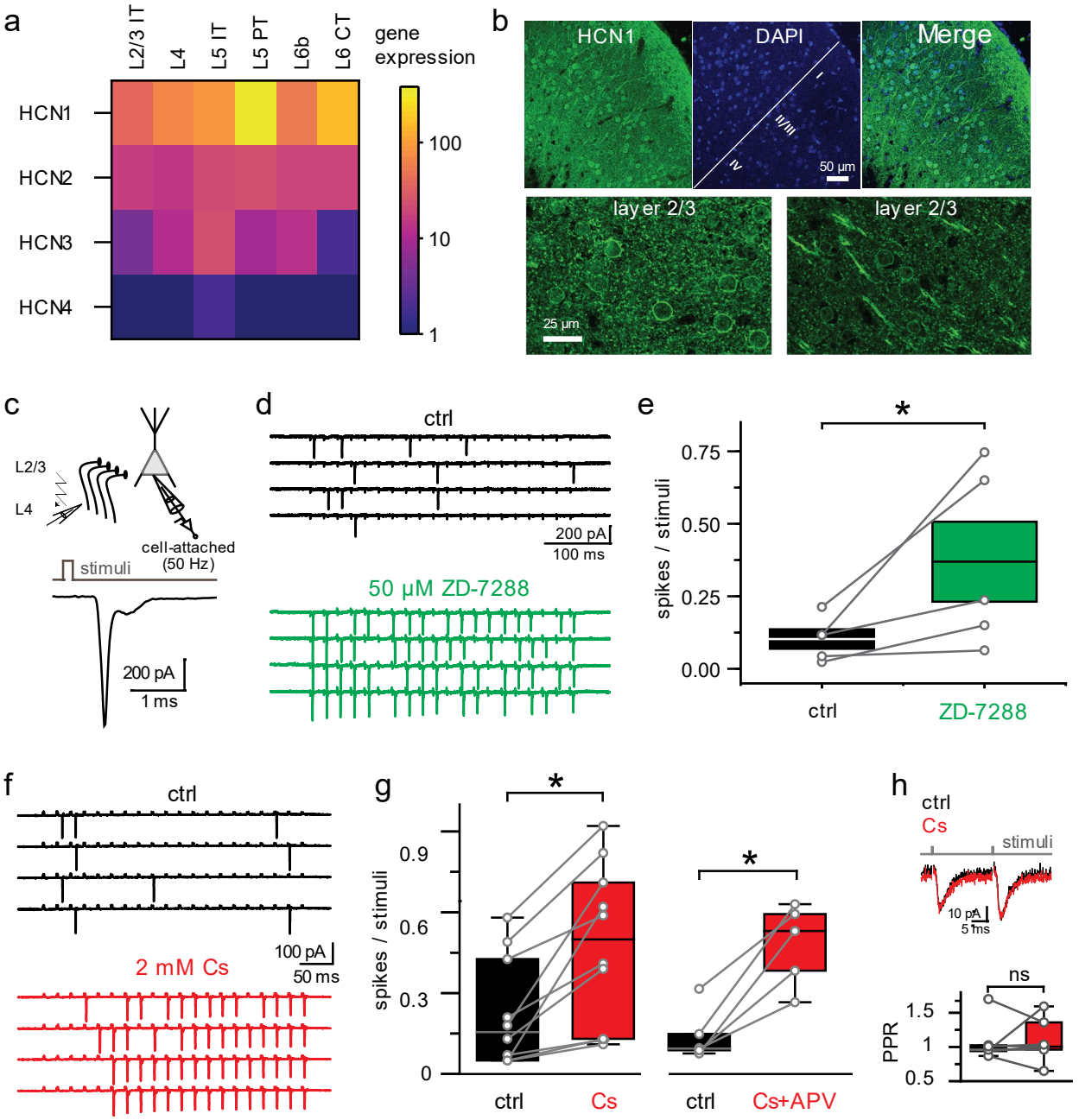

Fig 1. HCN expression and effect of Cs^+ on AP firing in cortical L2/3 PCs

a. HCN gene subunits show uniform expression pattern among cortical PC types. Data is collected from the online available dataset(29). **b.** HCN1 immunohistochemistry reveals dense somatic expression in layer 2/3 of the visual cortex **c.** HCN channels control the excitability of L2/3 PCs. Schematic illustration of the experimental arrangement of cell attached recordings during extracellular stimulation of L4, and the shape of the elicited action potential. **d.** Representative traces showing

increased firing upon ZD-7288 application. **e.** ZD-7288 increases the firing of L2/3 PCs upon electrical stimulation (0.1 ± 0.03 spikes/stimuli vs 0.4 ± 0.12 spikes/stimuli in control vs ZD-7288 application, respectively, p=0.04, t(4)=-3.0, Student's paired-sample t-test, n=5). **f.** Increased spiking of L2/3 PC upon blockade of HCN channels with 2 mM CsMeSO4 (right). **g.** Pharmacological block of I_h significantly increases the firing response of L2/3 PCs (0.22 ± 0.06 spikes/stimuli vs. 0.48 ± 0.09 spikes/stimuli for control vs CsMeSO4 bath application, p=0.002, t(9)=-4.42, Student's paired t-test, n=10. **h.** Presynaptic contributions were examined using the paired-pulse ratio (PPR) in whole cell current clamp recordings (1.09 ± 0.12 spikes/stimuli vs. 1.17 ± 0.15 spikes/stimuli for control vs CsMeSO4 bath application, p=0.422, t(6)=-0.8612, Student's paired t-test, n=7).

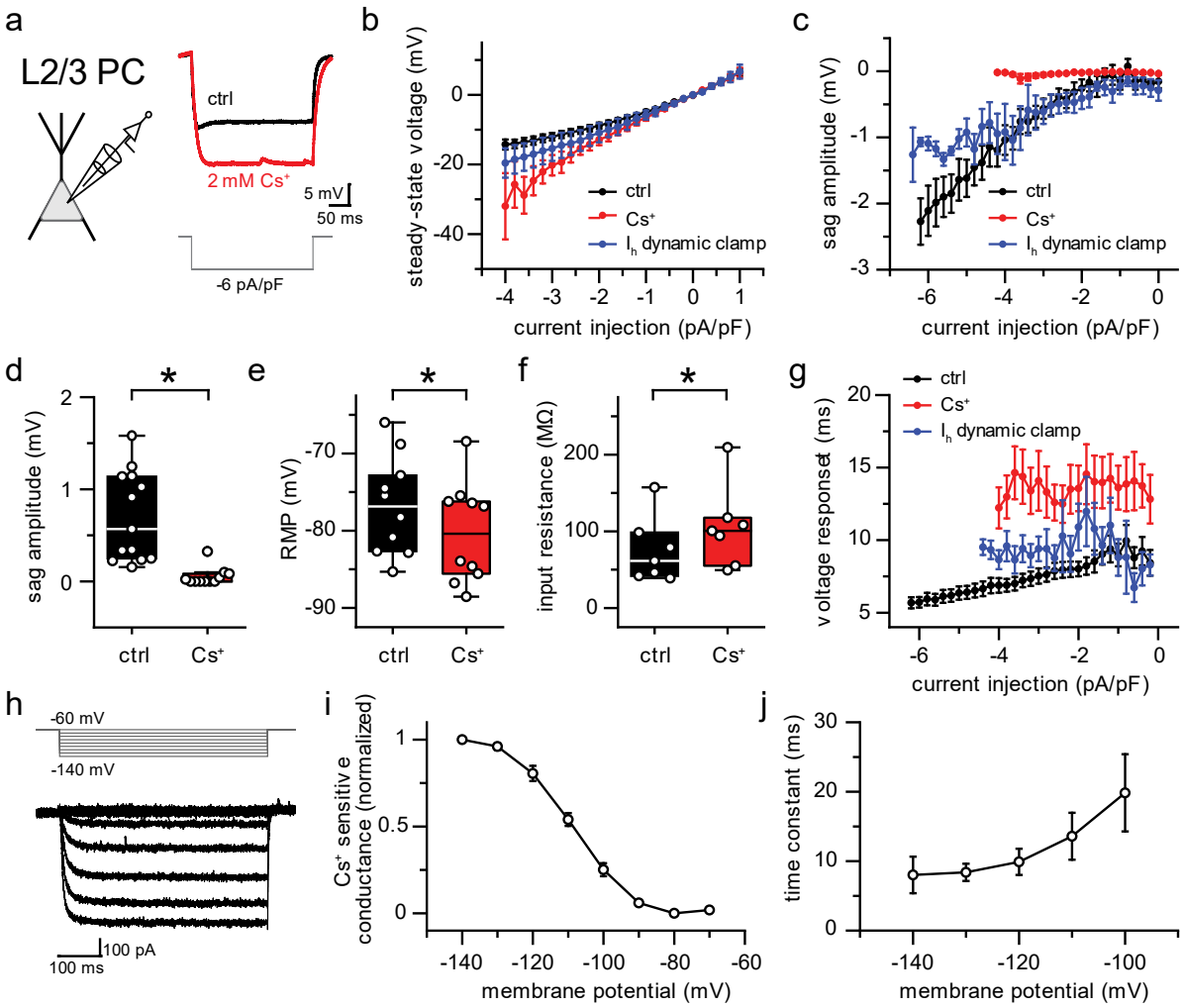

Fig 2. Functionally relevant I_h in L2/3 PCs

a. Whole cell current clamp recordings showing the presence and absence of sag response to very negative current commands in control conditions (black) and upon Cs^+ application (red). **b.** Steady-state voltage response rectification upon hyperpolarizing current injections is mediated by I_h. **c.** Sag voltage is abolished by blocking I_h. **d.** Sag amplitude is Cs^+ sensitive (0.7 ± 0.49 mV vs. 0.05 ± 0.1 mV for control vs CsMeSO4 application, $p=2.46^{-4}$, t(22)=4.37, Student's two-sample t-test, n=13 and 11). **e.** Resting membrane potential is modulated by I_h (-76.75 ± 6.37 mV vs. -80.29 ± 6.48 mV for control vs CsMeSO4 bath application, $p=1.98^{-4}$, t(9)=6.02, Student's paired t-test, n=10). **f.** Input resistance is altered by I_h (74.78 ± 42.34 mV vs. 104.99 ± 52.91 mV for control vs CsMeSO4 bath application, p=0.048, t(6)=-2.48, Student's paired t-test, n=7). **g.** The time course of voltage responses to hyperpolarizing current on the magnitude of the current injection is abolished by Cs^+. **h.** Example voltage clamp recording of cesium sensitive currents in a L2/3 PC. **i.** Voltage dependence of cesium sensitive current activation, **j.** Voltage dependent activation kinetics of cesium sensitive currents.

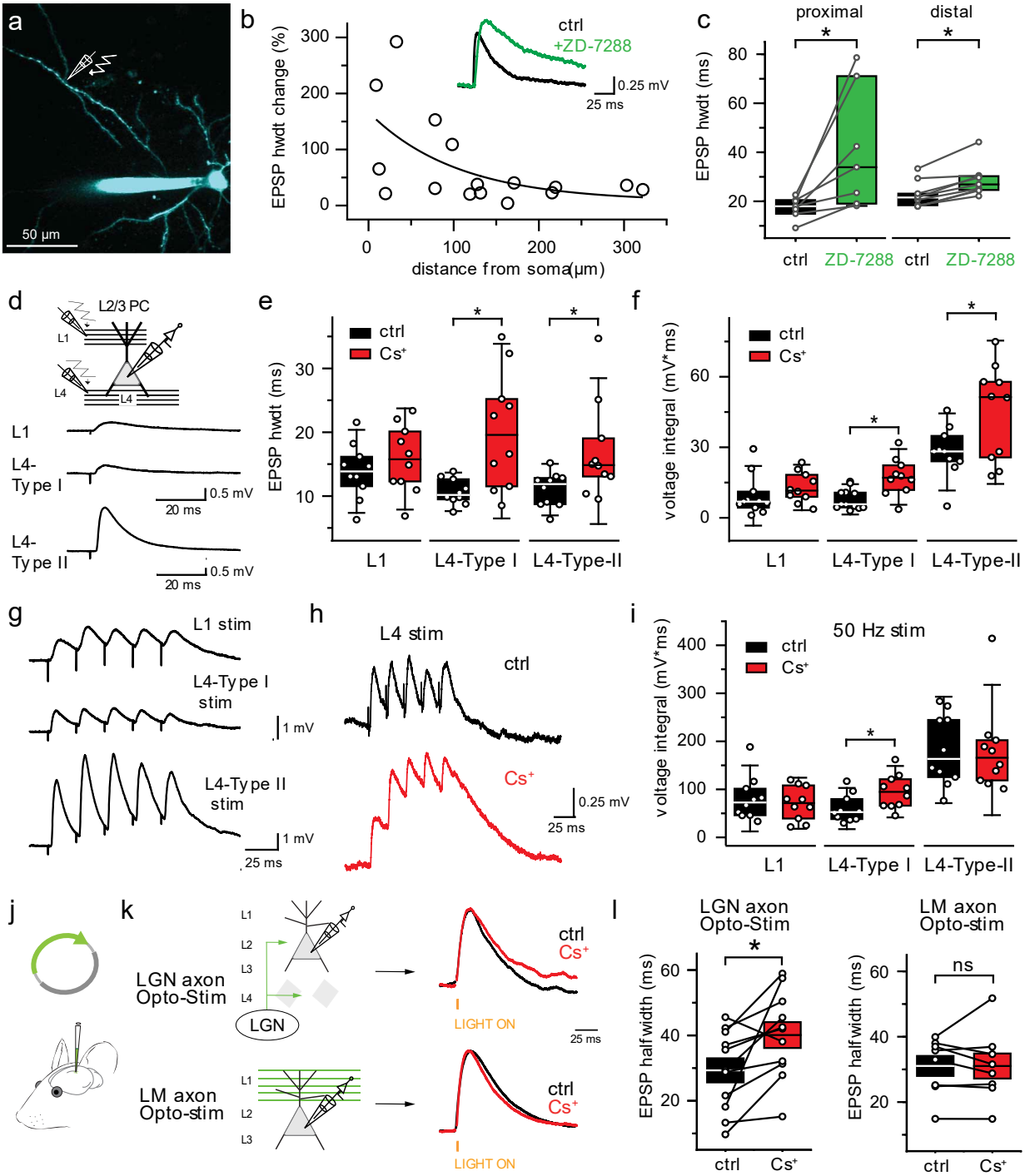

Fig 3. Noncanonical effect of I_h block on EPSPs in L2/3 PCs

a. Experimental arrangement of extracellular targeted stimulation of a L2/3 PC dendrite. **b.** Application of ZD-7288 revealed a proximal bias for EPSP modulation by I_h (Exponential fit τ=104.7 µm, R^2=0.33, n=18). Inset shows a stimulating location 28 µm away from the soma in control conditions (black trace) and upon Z-7288 application (green trace). **c.** EPSP halfwidth is significantly modulated along the

592 dendritic axis by I_h, (proximal dendritic locations: 17.42 ± 1.68 ms vs. 40.95 ± 24.78 ms for control vs
593 50µm ZD-7288 bath application, p=0.03, t(6)=2.84, Student's paired t-test, n=7, distal dendritic
594 locations: 22.68 ± 1.78 ms vs. 28.65 ± 2.17 ms for control vs 50µm ZD-7288 bath application, $p=2.1^{-}$
595 ^{4}, t(8)=-6.39, Student's paired t-test, n=9)**. d.** Schematic illustration of the experimental arrangement.
596 L2/3 PCs were recorded in whole-cell current clamp mode, and a stimulating electrode was placed
597 either in L1 or L4. **e.** I_h modulates EPSP halfwidth for L4 stimulation, but not for L1 (13.87 ± 1.37 ms
598 vs. 15.8 ± 1.67 ms for control vs CsMeSO4 bath application in L1, p=0.38, t(18)=-0.89, Student's two-
599 sample t-test, n=10 each, 10.65 ± 0.64 ms vs. 20.17 ± 2.88 ms for control vs CsMeSO4 bath application
600 for L4-Type I inputs, p=0.005, t(18)=-3.22, Student's two-sample t-test, n=10 each, 11.01 ± 0.85 ms
601 vs. 17.05 ± 2.41 ms for control vs CsMeSO4 bath application for L4-Type II, p=0.03, t(18)=-2.36,
602 Student's two-sample t-test, n=10 each). **f.** Pathway-specific I_h effect on unitary EPSP voltage integral
603 (9.35 ± 2.54 mV*ms vs. 12.9 ± 2.04 mV*ms for control vs CsMeSO4 bath application in L1, p=0.3,
604 t(19)=-1.07, Student's two-sample t-test, n=11 and n=10 respectively, 7.85 ± 1.24 mV*ms vs. 17.39 ±
605 2.5 mV*ms for control vs CsMeSO4 bath application for L4-Type I inputs, p=0.002, t(20)=-3.6,
606 Student's two-sample t-test, n=12 and n=10 respectively, 28.01 ± 3.45 mV*ms vs. 44.89 ± 6.42
607 mV*ms for control vs CsMeSO4 bath application for L4-Type II inputs, p=0.03, t(18)=-2.31, Student's
608 two-sample t-test, n=10 each). **g.** Representative recordings of 50 Hz repeated extracellular stimuli (L1
609 – grey, L4-Type I – blue, putative L4-Type II -green). **h.** Temporal summation of L4-Type I input
610 stimulation in control conditions (black) and during CsMeSO4 application (red). **i.** Pathway-specific
611 I_h modulation of synaptic summation (81.05 ± 14.5 mV*ms vs. 71.07 ± 11.19 mV*ms for control vs
612 CsMeSO4 bath application in L1, p=0.6, t(18)=0.54, Student's two-sample t-test, n=10 each, 60.06 ±
613 9.03 mV*ms vs. 95.15 ± 11.29 mV*ms for control vs CsMeSO4 bath application for L4-Type I,
614 p=0.03, t(18)=-2.42, Student's two-sample t-test, n=10 each, 182.08 ± 23.36 mV*ms vs. 182.05 ±
615 28.59 mV*ms for control vs CsMeSO4 bath application for L4-Type II, p=0.99, $t(18)=8.74*10^{-4}$,
616 Student's two-sample t-test, n=10 each). **j.** Schematic illustration of the experimental setup. Mice were
617 injected with AAV.CAMKII.C1V1/eYFP either in the latermodial visual area (LM, to label axons
618 arriving to L1) or in the LGN (to label proximal targeting axons). **k.** Example trace showing
619 optogenetic activation of LM (top) and LGN (bottom) axons in control conditions (black) and upon
620 Cs^+ application (red). Traces are normalized. Blue line marks the timing of the optogenetic stimulus.
621 **l.** Cs^+ effect on optogenetically elicited EPSPs from cortico-cortical (LM, left; 35.06 ± 3.06 vs. 31.04
622 ± 3.82 for control vs Cs^+ respectively, p=0.99, t(7)=0.001, Student's paired-sample t-test, n=8) and
623 thalamic (LGN, right; 29.31 ± 3.68 vs. 40.11 ± 3.95 for control vs Cs^+ respectively, p=0.01, t(10)=-
624 2.95, Student's paired-sample t-test, n=11) sources.

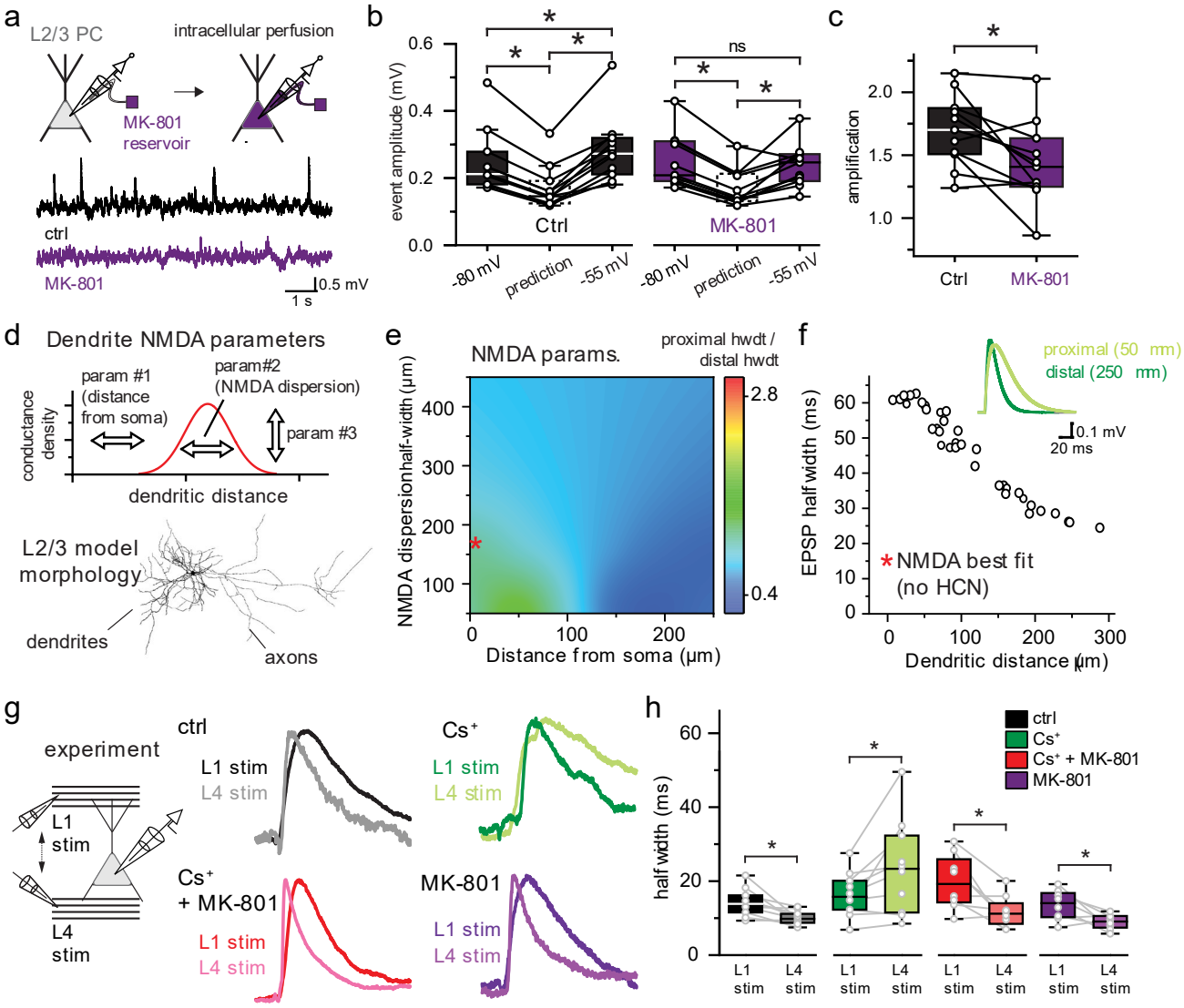

Fig 4. Pathway-specific NMDA receptor boosting of synaptic information

a. Schematic illustration of intracellular pipette solution perfusion during whole-cell patch clamp recordings. Briefly, the pipette was filled with control recording solution (black trace), which was exchanged to an intracellular solution containing 50 µM MK-801 (purple trace) during the recording. **b.** Mean peak amplitude of sEPSPs measured at two different membrane potentials and two different recording conditions (ctrl -80 mV vs. ctrl prediction: $p=4.72*10^{-6}$, $t(10) = 8.86$, ctrl -80 mV vs ctrl -55 mV: $p=0.02$, $t(10) = -2.81$, ctrl prediction vs ctrl -55 mV: $p=1.63*10^{-5}$, $t(10) = -7.71$, MK-801 -80 mV vs. MK-801 prediction: $p=1.15*10^{-6}$, $t(10) = 10.36$, MK-801 -80 mV vs MK-801 -55 mV: $p=0.58$, $t(10) = 0.57$, MK-801 prediction vs MK-801 -55 mV: $p=2.69*10^{-3}$, $t(10) = -3.95$, Student's paired-sample t-test, n = 11 for each). **c.** Synaptic amplification estimated by dividing the predicted peak

amplitude from the hyperpolarized recordings and the measured peak at depolarized membrane potentials (1.69 ± 0.09 and 1.43 ± 0.1 for ctrl and MK-801 amplification respectively, p=0.01, t(10) = 3.04, Student's paired-sample t-test, n=11). **d.** Schematic illustration of the multiparameter NEURON fitting procedure for dendritic NMDA. Conductance localization, dispersions, and conductance densities of NMDA were varied along a somato-dendritic axis as set by a Gaussian curve, which was shifted in space, in peak, and in width (top panel). Simulations were carried out using fully reconstructed L2/3 PC from the Allen Institute open-source database (bottom panel). **e.** Inserting NMDA receptors into proximally located simulated synapses recreated the experimentally determined distance-halfwidth relationship. Notice the best fit of the control conditions (where proximal/distal EPSP halfwidth is similar), is characterized by a Gaussian curve with proximal peak center with a moderate width (dispersion). **f.** Best fit of the distance-dependent EPSP halfwidth with no HCN in the system. Red asterisk denotes the best fit parameter-space on panel. Proximally (gray) and distally (black) originating EPSPs from the model are shown in the inset. **e. g.** Amplitude-normalized EPSPs recorded from L2/3 PCs by minimal stimulation in either in L1 (dark color tones) or L4 (light color tones) in different recording conditions (ctrl: *black*, extracellular cesium: *green*, extracellular cesium + intracellular MK-801: *red*, intracellular MK-801: *purple*). Cells were recorded for each pharmacological condition independently with L4 and L1 stimulation occurring in each recording. **h.** As predicted (panel f) proximal inputs from L4-originating EPSPs were faster than those from distal L1 synapses in control conditions. The broadening effect of cesium on L4 (proximal) originating EPSPs is occluded by NMDA receptor block (14.25 ± 1.17 ms and 10.11 ± 0.56 ms for L1 vs L4 stimuli in control conditions, $p=6.73*10^{-3}$, t(9)=3.5, Student's paired-sample t-test, n=10 each, 16.22 ± 1.91 ms and 23.61 ± 4.04 ms for L1 vs L4 stimuli during Cs bath application, p=0.03, t(9)=-2.67, Student's paired-sample t-test, n=10 each, 19.92 ± 2.65 ms and 11.8 ± 1.55 ms for L1 vs L4 stimuli during Cs bath application and MK-801 intracellular application, p=0.02, t(7)=3.01, Student's paired-sample t-test, n=8 each, 13.62 ± 1.43 ms and 8.97 ± 0.72 ms for L1 vs L4 stimuli during MK-801 intracellular application, p=0.025, t(7)=2.84, Student's paired-sample t-test, n=8 each).

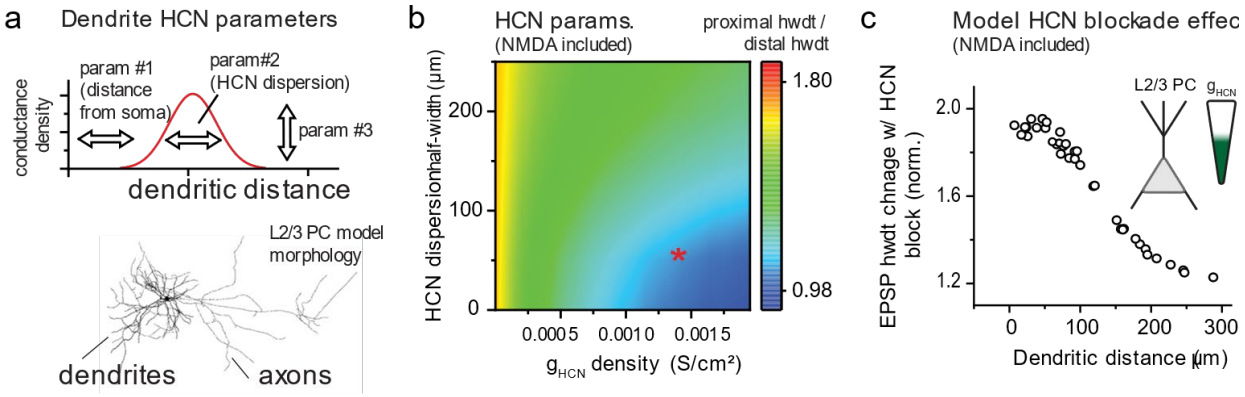

Fig 5. Proximal bias in HCN channel expression dampens proximal NMDA receptor-dependent synaptic boosting in a NEURON model simulation.

a. Schematic illustration of the multiparameter NEURON fitting procedure for dendritic HCN. Simulations here included the NMDA dendritic parameters established in Fig. 4. HCN conductance localization, dispersions, and conductance densities were varied along the somato-dendritic axis as set by a Gaussian curve, which was shifted in space, in peak, and in width as well (top panel). Simulations were carried out using fully reconstructed L2/3 PC from the Allen Institute open-source database (bottom panel). **b**. A proximal abundance bias of HCN channels recapitulates experimental findings in control conditions. Best fit in the parameter space tested is denoted with red asterisk, where a high density of HCN channels were proximally localized. **c.** Model-derived data showing the effect of HCN blockade in the best-fit scheme when NMDA is also included as shown in Fig. 4. Note that the effect of HCN removal in this model closely recapitulates our experimental findings using ZD-7288 earlier.

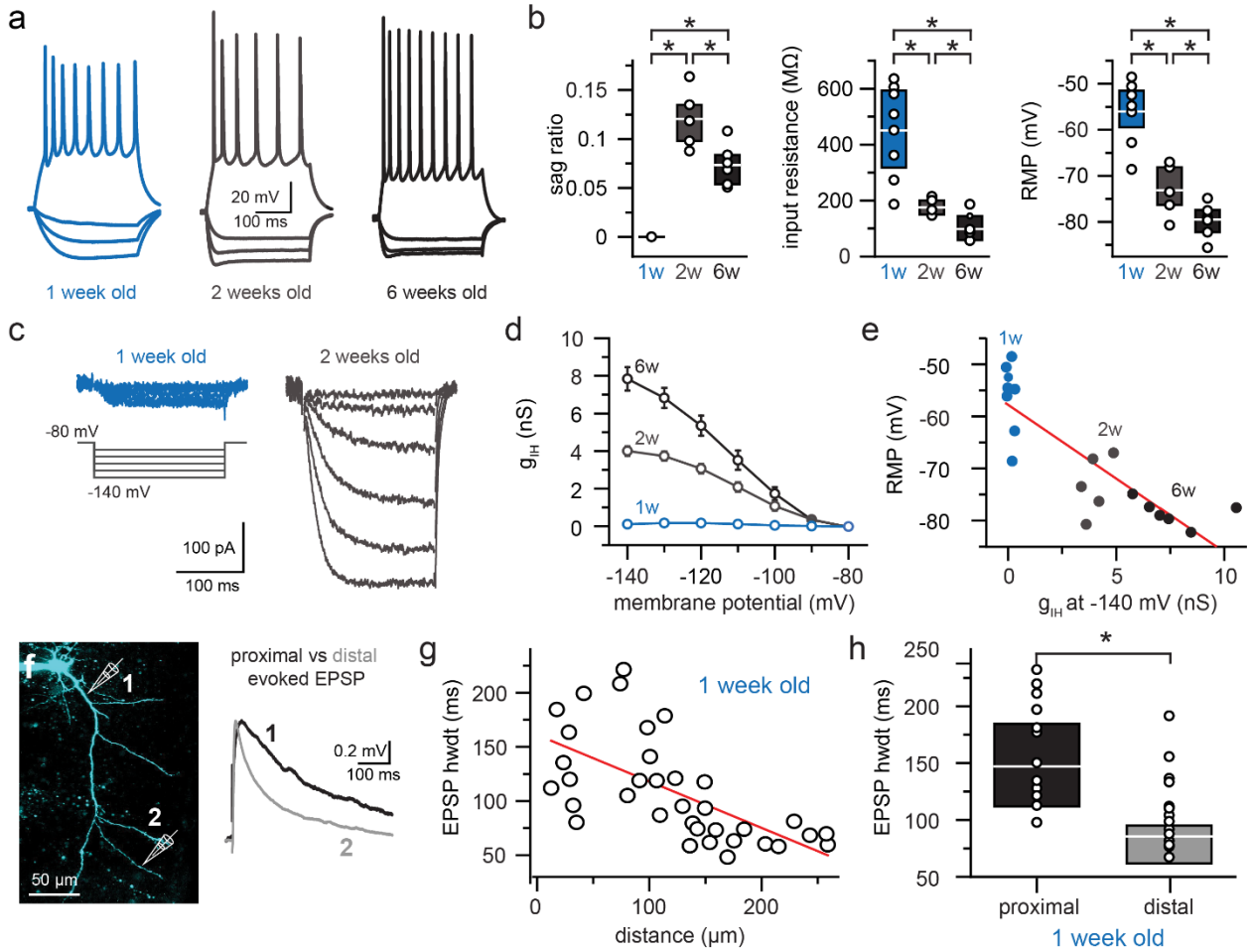

Fig 6. Developmental regulation of I_h expression

a. Representative firing patterns recorded from one week old (left, blue), two weeks old (middle, grey) and six weeks old L2/3 PCs. **b.** Developmental regulation of sag ratio (0.0 ± 0.0, 0.12 ± 0.01 and 0.07 ± 0.01 for one- (n=8), two- (n=5) and six week old L2/3 PCs (n=6), respectively, p=0 for one week old vs two weeks old cells, p=0.01, t(9)=3.04 for two vs six weeks old cells and p=0 for one vs six weeks old cells, Student's two-sample t-test), input resistance (450.6 ± 57.91 MΩ, 175.66 ± 13.66 MΩ and 98.34 ± 18.86 MΩ for one- (n=8), two- (n=5) and six week old L2/3 PCs (n=7), respectively, p=0.004, t(11)=3.65 for one week old vs two weeks old cells, p=0.01, t(10)=3.06 for two vs six weeks old cells and p=1.11*10^{-4}, t(13)=5.54 for one vs six weeks old cells, Student's two-sample t-test) and resting membrane potential (-56.05 ± 2.33 mV, -73.13 ± 2.55 mV and -79.47 ± 1.33 MΩ for one- (n=8), two- (n=5) and six week old L2/3 PCs (n=7), respectively, p=5.9*10^{-4}, t(11)=4.76 for one week old vs two weeks old cells, p=0.04, t(10)=2.39 for two vs six weeks old cells and p=1.36*10^{-6}, t(13)=8.37 for one vs six weeks old cells, Student's two-sample t-test). **c.** Representative voltage clamp recordings of

hyperpolarization activated currents in one week old (left, blue), two weeks old (middle, gray) and six weeks old L2/3 PCs (right, black). **d.** Voltage dependence of hyperpolarization activated currents in one week old (blue), two weeks old (gray) and six weeks old L2/3 PCs (black). **e.** Negative correlation between measured hyperpolarization activated current and resting membrane potential during development (Linear fit (red) slope: -2.84 mV/nS, intercept: -57.67 mV, R^2=0.71, n=20). **f.** Two-photon microscopy image depicting a proximal and a distal extracellular stimulating location positioned closely to an Alexa-594 filled L2/3 PC dendrite (left), and the resulting EPSPs (proximal – black, distal – green). **g.** EPSP halfwidth decreases with dendritic distance (Linear fit (red) slope: -0.42 ms/µm, intercept: 161.01 ms, R^2=0.4, n=35). **h.** EPSPs were significantly slower in proximal dendritic locations (147.07 ± 12.87 ms and 85.57 ± 6.83 ms for proximal and distal events, respectively, $p=5.31*10^{-5}$, t(33)=4.64, Student's two-sample t-test, n=13 and 22, respectively).

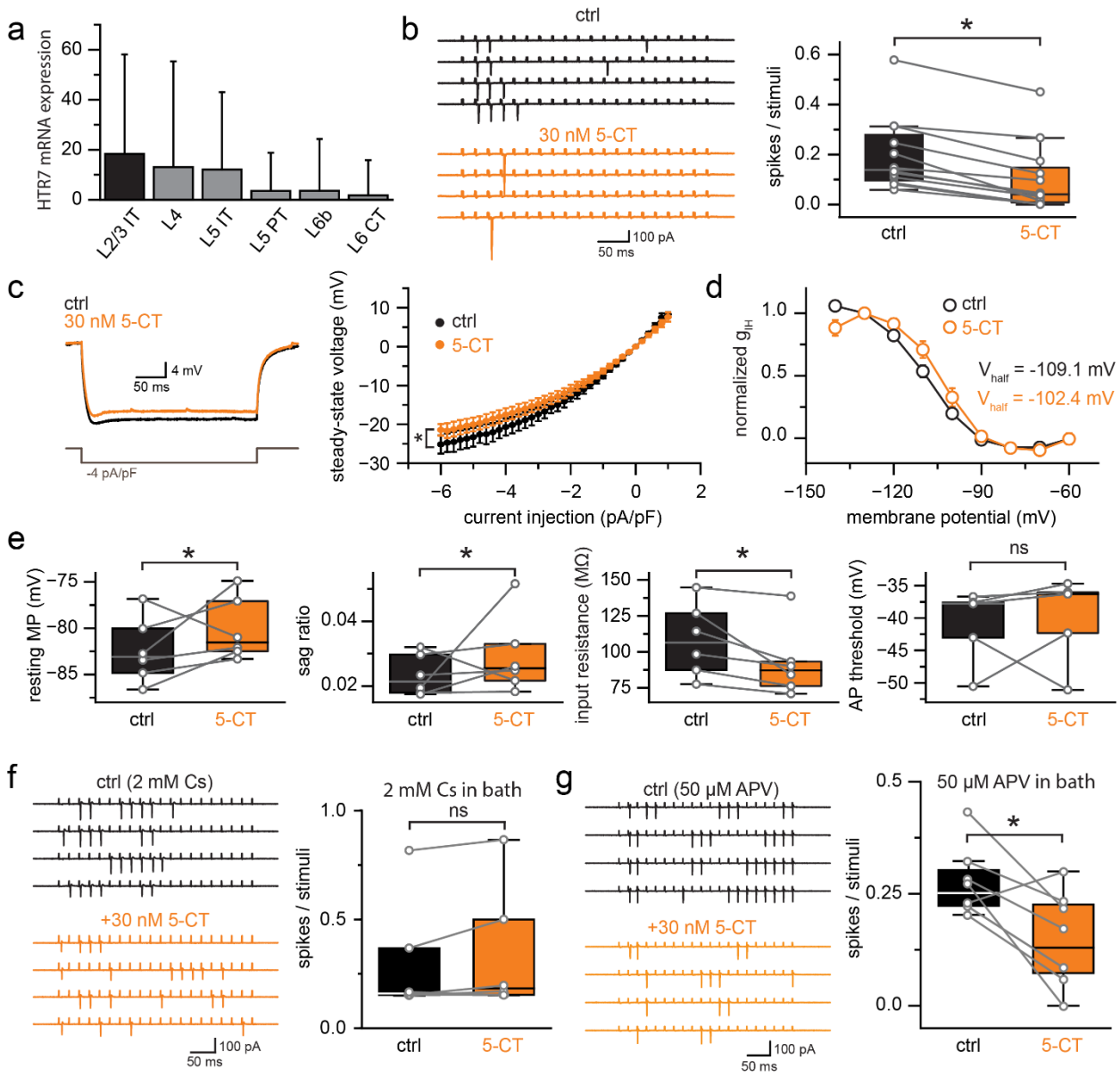

Fig 7. Neuromodulation shifts L2/3 PC excitability via HCN channels

a. $5HT_7$ receptor mRNA is abundantly expressed in L2/3 PCs. Data is collected from the online available dataset(29). **b.** Example cell attached recording of a L2/3 PC (left) upon 50 Hz extracellular stimulation in L4 in control conditions (black) and 5-CT bath application (orange). 5-CT significantly reduced L2/3 PC spiking (0.2 ± 0.04 spike/stimuli vs. 0.1 ± 0.04 spike/stimuli for control vs 5-CT application, $p=3.57*10^{-6}$, t(11)=7.92, Student's paired-sample t-test, n=12 each) **c.** Example current clamp recording of voltage responses to hyperpolarizing current injections (left; control – black, 5-CT – orange). Steady-state voltage response rectification is amplified by $5HT_7R$ blockade (right). **d.** 5-CT shifts the voltage dependence of hyperpolarization activated currents (-109.06 ± 0.47 mV vs -102.35

± 1.09 mV half activation for control vs 5-CT bath application, R^2 = 0.99 for both). **e.** 5-CT did not alter resting membrane potential (-82.41 ± 1.43 mV vs -80.14 ± 1.38 mV in control vs 5-CT bath application, respectively, p=0.89, t(5)=-1.41, Student's paired-sample t-test, n=6 each), sag ratio at -2 pA/pF current injection (0.02 ± $2.55*10^{-3}$ vs 0.03 ± 0.01 in control vs 5-CT bath application, respectively, p=0.82, t(5)=-1.01, Student's paired-sample t-test, n=6 each) and action potential threshold (-41.13 ± 2.6 mV, -40.08 ± 3.05 mV in control vs 5-CT bath application, respectively, p=0.64, t(4)=-0.4, Student's paired-sample t-test, n=5 each), but significantly reduced input resistance (108.21± 10.3 mΩ, 92.29 ± 9.9 MΩ in control vs 5-CT bath application, respectively, p=0.02, t(5)=2.75, Student's paired-sample t-test, n=6 each). **f.** Example recording showing no effect of 5-CT bath application when HCN channels were blocked (left: example recordings, right: 0.3 ± 0.11 spike/stimuli vs 0.34 ± 0.12 spike/stimuli in control vs 5-CT bath application, respectively, p=0.13, t(5)=-1.81, Student's paired-sample t-test, n=6 each). **g.** NMDA independent 5-CT effect on L2/3 PC excitability (0.27 ± 0.03 spike/stimuli vs 0.14 ± 0.04 spike/stimuli in control vs 5-CT bath application, respectively, p=0.01, t(7)=3.66, Student's paired-sample t-test, n=7 each).

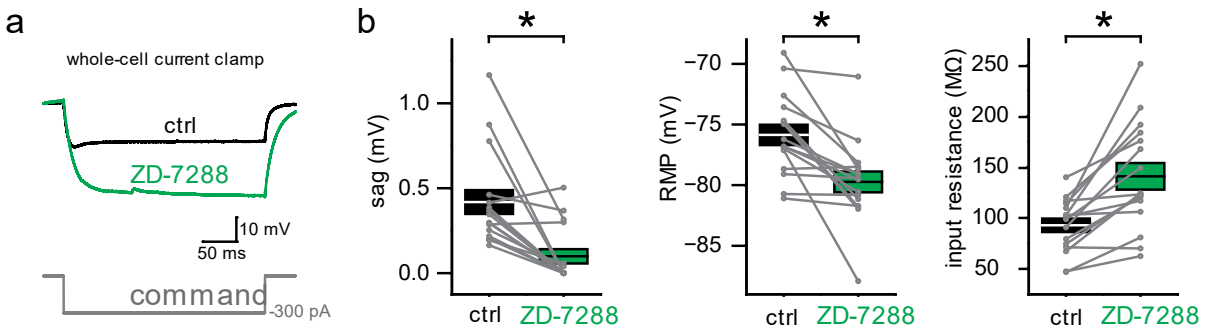

Supplementary Figure 1. ZD-7288 application results in similar active and passive electrical alterations.

a. Representative effect of ZD-7288 on voltage responses to hyperpolarizing current injections. **b.** ZD-7288 abolished sag voltage (0.42 ± 0.07 mV vs 0.1 ± 0.04 mV in control vs ZD-7288 application, respectively, $p=4.5*10^{-4}$, t(15)=4.47, Student's paired-sample t-test, n=16), decreased the resting membrane potential (-75.86 ± 0.84 mV vs -79.73 ± 0.86 mV in control vs ZD-7288 application, respectively, $p=4.41*10^{-4}$, t(15)=4.48, Student's paired-sample t-test, n=16), and increased the input resistance (92.74 ± 6.59 MΩ vs 140.8 ± 13.07 MΩ in control vs ZD-7288 application, respectively, $p=1.79*10^{-4}$, t(15)=-4.93, Student's paired-sample t-test, n=16).

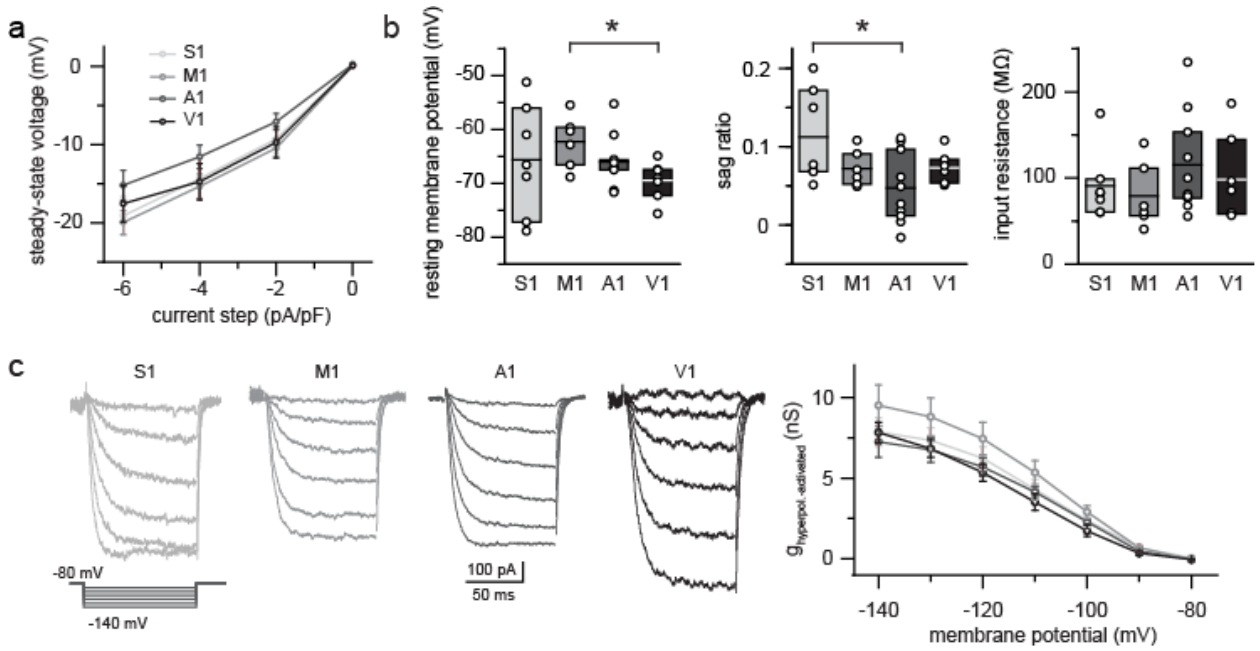

Supplementary Figure 2. Similar Ih current and effect in different cortical areas.

a. Steady-state rectification of L2/3 PCs in the primary somatosensory cortex (S1), primary motor cortex (M1), primary auditory cortex (A1) and primary visual cortex (V1). **b.** Similar resting membrane potential (left), sag ratio (middle) and input resistance (right) of L2/3 PCs in different cortical areas. **c.** Example hyperpolarization activated current recordings from four cortical areas (left), with similar voltage dependent activation (right).

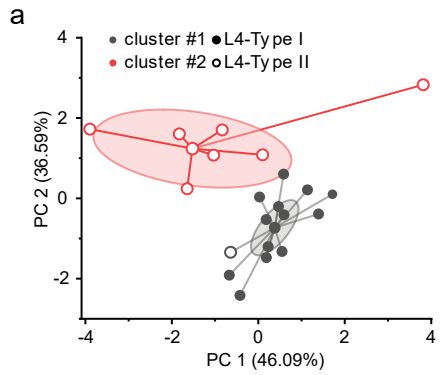

Supplementary Figure 3. L4-Type I and L4-Type II inputs are well separated by k-means clustering

k-means clustering results plotted along the first and second principal component. Ellipses denote the confidence interval; edges are connected to the cluster center. Hollow circles represent L4 Type II inputs and filled circles represent L4-Type I inputs determined by the experimenter.

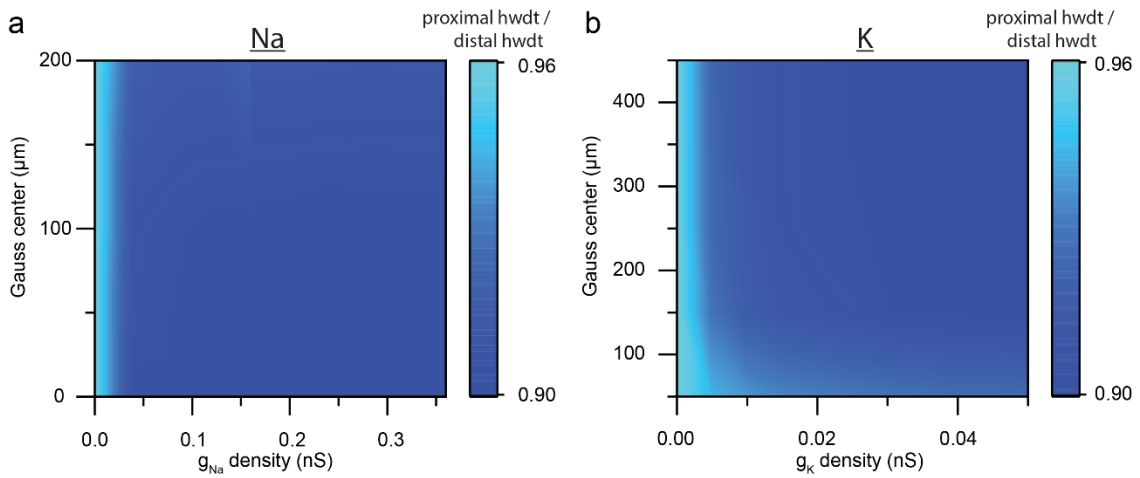

Supplementary Figure 4. The presence of dendritic sodium and potassium channels cannot explain wider proximal synaptic inputs

a. Sodium channels cannot explain the distance-EPSP halfwidth relationship observed when I_h was blocked. Color coding denotes the ratio between proximal and distal EPSP halfwidths. Notice the miniscule range of the color coding. **C.** Same as panel **b.** but for voltage dependent potassium channels.

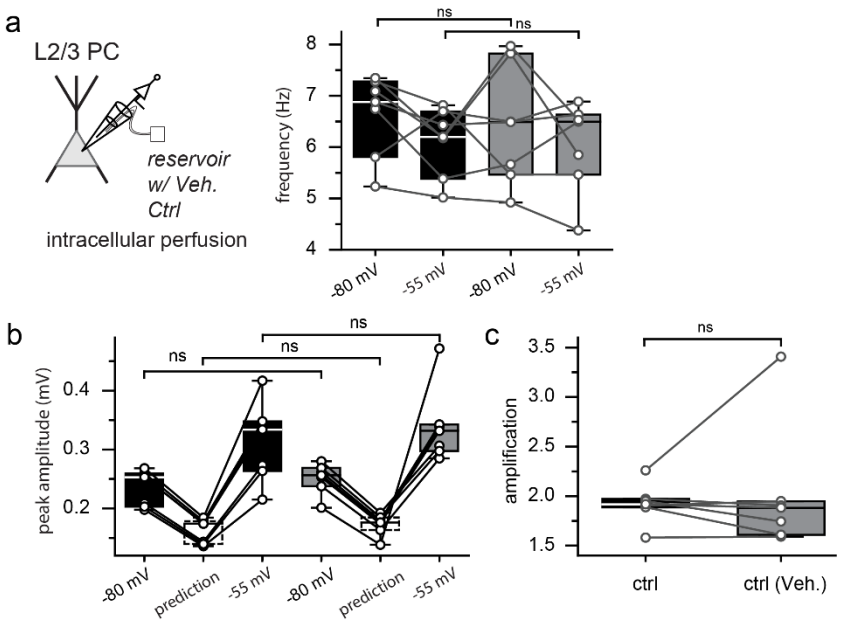

Supplementary Figure 5. Pipette perfusion does not alter spontaneous circuit activity measurements

a. sEPSP frequency is unaltered by pipette perfusion (6.63 ± 0.3 and 6.4 ± 0.44 for ctrl -80 mV and perfused ctrl -80 mV, p=0.57, t(6) = 0.59, 6.1 ± 0.25 and 6.03 ± 0.33 for ctrl -55 mV and perfused ctrl -55 mV, p=0.83, t(6) = 0.23, n=7 for each, Student's paired-sample t-test). **b.** sEPSP peak amplitudes are stable during pipette perfusion experiments (0.23 ± 0.01 and 0.25 ± 0.01 for ctrl -80 mV and perfused ctrl -80 mV, p=0.43, t(6) = -0.83, 0.16 ± 0.01 and 0.17 ± 0.01 for ctrl prediction and perfused prediction, p=0.43, t(6) =-0.83, 0.31 ± 0.03 and 0.34 ± 0.02 for ctrl -55 mV and perfused ctrl -55 mV, p=0.24, t(6) = -1.31, n=7 each, Student's paired-sample t-test). **c.** Pipette perfusion does not alter measured synaptic amplification (1.92 ± 0.07 and 2.01 ± 0.24 for ctrl and perfused ctrl, p=0.65, t(6) = -0.48, n=7 each, Student's paired-sample t-test).

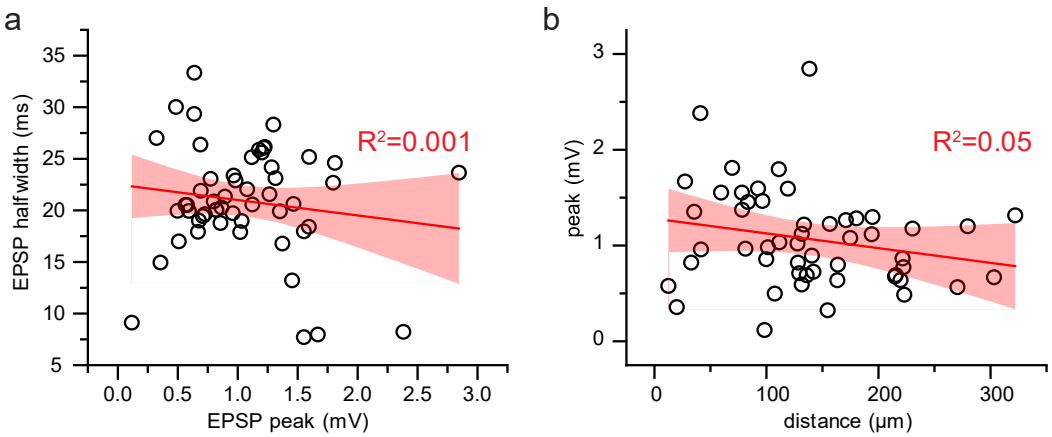

Supplementary Figure 6. Elicited EPSP halfwidth in not dependent on event amplitude

a. EPSPs elicited by electrical stimulation show no correlation between event amplitude and halfwidth (R^2= 0.021, n=53). **b.** EPSP peak is not dependent on dendritic distance from the soma (R^2= 0.021, n=53).

REFERENCES

1. Quiquempoix M, Fayad SL, Boutourlinsky K, Leresche N, Lambert RC, Bessaih T. Layer 2/3 pyramidal neurons control the gain of cortical output. Cell reports. 2018;24(11):2799-807. e4.
2. Wilson DE, Whitney DE, Scholl B, Fitzpatrick D. Orientation selectivity and the functional clustering of synaptic inputs in primary visual cortex. Nature neuroscience. 2016;19(8):1003-9.
3. Hage TA, Bosma-Moody A, Baker CA, Kratz MB, Campagnola L, Jarsky T, et al. Synaptic connectivity to L2/3 of primary visual cortex measured by two-photon optogenetic stimulation. Elife. 2022;11:e71103.
4. Ding Z, Fahey PG, Papadopoulos S, Wang E, Celii B, Papadopoulos C, et al. Functional connectomics reveals general wiring rule in mouse visual cortex. bioRxiv. 2023:2023.03. 13.531369.
5. Scholl B, Wilson DE, Jaepel J, Fitzpatrick D. Functional logic of layer 2/3 inhibitory connectivity in the ferret visual cortex. Neuron. 2019;104(3):451-7. e3.
6. Scholl B, Fitzpatrick D. Cortical synaptic architecture supports flexible sensory computations. Current opinion in neurobiology. 2020;64:41-5.
7. Goetz L, Roth A, Häusser M. Active dendrites enable strong but sparse inputs to determine orientation selectivity. Proceedings of the National Academy of Sciences. 2021;118(30):e2017339118.
8. Smith SL, Smith IT, Branco T, Häusser M. Dendritic spikes enhance stimulus selectivity in cortical neurons in vivo. Nature. 2013;503(7474):115-20.
9. Ujfalussy BB, Makara JK, Lengyel M, Branco T. Global and multiplexed dendritic computations under in vivo-like conditions. Neuron. 2018;100(3):579-92. e5.
10. Landau AT, Park P, Wong-Campos JD, Tian H, Cohen AE, Sabatini BL. Dendritic branch structure compartmentalizes voltage-dependent calcium influx in cortical layer 2/3 pyramidal cells. Elife. 2022;11:e76993.
11. Ferrarese L, Jouhanneau J-S, Remme MW, Kremkow J, Katona G, Rózsa B, et al. Dendrite-specific amplification of weak synaptic input during network activity in vivo. Cell reports. 2018;24(13):3455-65. e5.
12. Luo H, Hasegawa K, Liu M, Song W-J. Comparison of the upper marginal neurons of cortical layer 2 with layer 2/3 pyramidal neurons in mouse temporal cortex. Frontiers in Neuroanatomy. 2017;11:115.
13. Stuart GJ, Spruston N. Dendritic integration: 60 years of progress. Nature neuroscience. 2015;18(12):1713-21.
14. Takahashi N, Oertner TG, Hegemann P, Larkum ME. Active cortical dendrites modulate perception. Science. 2016;354(6319):1587-90.
15. Suzuki M, Larkum ME. General anesthesia decouples cortical pyramidal neurons. Cell. 2020;180(4):666-76. e13.
16. Wahl-Schott C, Biel M. HCN channels: structure, cellular regulation and physiological function. Cellular and molecular life sciences. 2009;66:470-94.
17. Xu N-l, Harnett MT, Williams SR, Huber D, O'Connor DH, Svoboda K, et al. Nonlinear dendritic integration of sensory and motor input during an active sensing task. Nature. 2012;492(7428):247-51.
18. Shah MM. Cortical HCN channels: function, trafficking and plasticity. The Journal of physiology. 2014;592(13):2711-9.
19. Lörincz A, Notomi T, Tamás G, Shigemoto R, Nusser Z. Polarized and compartment-dependent distribution of HCN1 in pyramidal cell dendrites. Nature neuroscience. 2002;5(11):1185-93.
20. Benarroch EE. HCN channels: function and clinical implications. Neurology. 2013;80(3):304-10.
21. Nolan MF, Dudman JT, Dodson PD, Santoro B. HCN1 channels control resting and active integrative properties of stellate cells from layer II of the entorhinal cortex. Journal of Neuroscience. 2007;27(46):12440-51.

22. Kalmbach BE, Buchin A, Long B, Close J, Nandi A, Miller JA, et al. h-Channels contribute to divergent intrinsic membrane properties of supragranular pyramidal neurons in human versus mouse cerebral cortex. Neuron. 2018;100(5):1194-208. e5.
23. Routh BN, Brager DH, Johnston D. Ionic and morphological contributions to the variable gain of membrane responses in layer 2/3 pyramidal neurons of mouse primary visual cortex. Journal of Neurophysiology. 2022;128(4):1040-50.
24. Datta D, Perone I, Morozov YM, Arellano J, Duque A, Rakic P, et al. Localization of PDE4D, HCN1 channels, and mGluR3 in rhesus macaque entorhinal cortex may confer vulnerability in Alzheimer's disease. Cerebral Cortex. 2023;33(24):11501-16.
25. Paspalas CD, Wang M, Arnsten AF. Constellation of HCN channels and cAMP regulating proteins in dendritic spines of the primate prefrontal cortex: potential substrate for working memory deficits in schizophrenia. Cerebral cortex. 2013;23(7):1643-54.
26. Foehring R, Waters R. Contributions of low-threshold calcium current and anomalous rectifier (Ih) to slow depolarizations underlying burst firing in human neocortical neurons in vitro. Neuroscience letters. 1991;124(1):17-21.
27. Bullis JB, Jones TD, Poolos NP. Reversed somatodendritic Ih gradient in a class of rat hippocampal neurons with pyramidal morphology. The Journal of physiology. 2007;579(2):431-43.
28. Williams SR, Stuart GJ. Site independence of EPSP time course is mediated by dendritic I h in neocortical pyramidal neurons. Journal of neurophysiology. 2000;83(5):3177-82.
29. Gouwens NW, Sorensen SA, Baftizadeh F, Budzillo A, Lee BR, Jarsky T, et al. Integrated morphoelectric and transcriptomic classification of cortical GABAergic cells. Cell. 2020;183(4):935-53. e19.
30. Larkum ME, Waters J, Sakmann B, Helmchen F. Dendritic spikes in apical dendrites of neocortical layer 2/3 pyramidal neurons. Journal of Neuroscience. 2007;27(34):8999-9008.
31. Harnett MT, Magee JC, Williams SR. Distribution and function of HCN channels in the apical dendritic tuft of neocortical pyramidal neurons. Journal of Neuroscience. 2015;35(3):1024-37.
32. Magee JC. Dendritic Ih normalizes temporal summation in hippocampal CA1 neurons. Nature neuroscience. 1999;2(6):508-14.
33. Vetter P, Roth A, Häusser M. Propagation of action potentials in dendrites depends on dendritic morphology. Journal of neurophysiology. 2001;85(2):926-37.
34. Malinow R. Transmission between pairs of hippocampal slice neurons: quantal levels, oscillations, and LTP. Science. 1991;252(5006):722-4.
35. Yang W, Carrasquillo Y, Hooks BM, Nerbonne JM, Burkhalter A. Distinct balance of excitation and inhibition in an interareal feedforward and feedback circuit of mouse visual cortex. Journal of Neuroscience. 2013;33(44):17373-84.
36. Balcioglu A, Gillani R, Doron M, Burnell K, Ku T, Erisir A, et al. Mapping thalamic innervation to individual l2/3 pyramidal neurons and modeling their 'readout'of visual input. Nature Neuroscience. 2023;26(3):470-80.
37. Sermet BS, Truschow P, Feyerabend M, Mayrhofer JM, Oram TB, Yizhar O, et al. Pathway-, layer- and cell-type-specific thalamic input to mouse barrel cortex. elife. 2019;8:e52665.
38. D'Souza RD, Wang Q, Ji W, Meier AM, Kennedy H, Knoblauch K, et al. Hierarchical and nonhierarchical features of the mouse visual cortical network. Nature communications. 2022;13(1):503.
39. Shen S, Jiang X, Scala F, Fu J, Fahey P, Kobak D, et al. Distinct organization of two cortico-cortical feedback pathways. Nature communications. 2022;13(1):6389.
40. Kondo S, Kiyohara Y, Ohki K. Response Selectivity of the Lateral Posterior Nucleus Axons Projecting to the Mouse Primary Visual Cortex. Frontiers in Neural Circuits. 2022;16:825735.
41. Zhuang J, Larsen RS, Takasaki KT, Ouellette ND, Daigle TL, Tasic B, et al. The spatial structure of feedforward information in mouse primary visual cortex. Biorxiv. 2019:2019.12. 24.888156.

42. London M, Hausser M. Dendritic computation. Annual review of neuroscience. 2005;28(1):503-32.
43. Berger T, Senn W, Lüscher H-R. Hyperpolarization-activated current I h disconnects somatic and dendritic spike initiation zones in layer V pyramidal neurons. Journal of neurophysiology. 2003;90(4):2428-37.
44. Tsay D, Dudman JT, Siegelbaum SA. HCN1 channels constrain synaptically evoked Ca2+ spikes in distal dendrites of CA1 pyramidal neurons. Neuron. 2007;56(6):1076-89.
45. Billeh YN, Cai B, Gratiy SL, Dai K, Iyer R, Gouwens NW, et al. Systematic integration of structural and functional data into multi-scale models of mouse primary visual cortex. Neuron. 2020;106(3):388-403. e18.
46. Palmer LM, Shai AS, Reeve JE, Anderson HL, Paulsen O, Larkum ME. NMDA spikes enhance action potential generation during sensory input. Nature neuroscience. 2014;17(3):383-90.
47. Branco T, Häusser M. Synaptic integration gradients in single cortical pyramidal cell dendrites. Neuron. 2011;69(5):885-92.
48. Bucurenciu I, Kulik A, Schwaller B, Frotscher M, Jonas P. Nanodomain coupling between Ca2+ channels and Ca2+ sensors promotes fast and efficient transmitter release at a cortical GABAergic synapse. Neuron. 2008;57(4):536-45.
49. Cornford JH, Mercier MS, Leite M, Magloire V, Häusser M, Kullmann DM. Dendritic NMDA receptors in parvalbumin neurons enable strong and stable neuronal assemblies. Elife. 2019;8:e49872.
50. Dodt HU, Frick A, Kampe K, Zieglgänsberger W. NMDA and AMPA receptors on neocortical neurons are differentially distributed. European journal of Neuroscience. 1998;10(11):3351-7.
51. Rowan MJ, Christie JM. Rapid state-dependent alteration in Kv3 channel availability drives flexible synaptic signaling dependent on somatic subthreshold depolarization. Cell reports. 2017;18(8):2018-29.
52. Guet-McCreight A, Chameh HM, Mahallati S, Wishart M, Tripathy SJ, Valiante TA, et al. Age-dependent increased sag amplitude in human pyramidal neurons dampens baseline cortical activity. Cerebral Cortex. 2023;33(8):4360-73.
53. Santello M, Nevian T. Dysfunction of cortical dendritic integration in neuropathic pain reversed by serotoninergic neuromodulation. Neuron. 2015;86(1):233-46.
54. Dori I, Dinopoulos A, Blue M, Parnavelas J. Regional differences in the ontogeny of the serotonergic projection to the cerebral cortex. Experimental neurology. 1996;138(1):1-14.
55. Vasefi MS, Yang K, Li J, Kruk JS, Heikkila JJ, Jackson MF, et al. Acute 5-HT7 receptor activation increases NMDA-evoked currents and differentially alters NMDA receptor subunit phosphorylation and trafficking in hippocampal neurons. Molecular brain. 2013;6:1-9.
56. Megıas M, Emri Z, Freund T, Gulyas A. Total number and distribution of inhibitory and excitatory synapses on hippocampal CA1 pyramidal cells. Neuroscience. 2001;102(3):527-40.
57. Nevian T, Larkum ME, Polsky A, Schiller J. Properties of basal dendrites of layer 5 pyramidal neurons: a direct patch-clamp recording study. Nature neuroscience. 2007;10(2):206-14.
58. Hubel DH, Wiesel TN. Brain mechanisms of vision. Scientific American. 1979;241(3):150-63.
59. Hubel DH, Wiesel TN. Brain and visual perception: the story of a 25-year collaboration: Oxford University Press; 2004.
60. Scholl B, Thomas CI, Ryan MA, Kamasawa N, Fitzpatrick D. Cortical response selectivity derives from strength in numbers of synapses. Nature. 2021;590(7844):111-4.
61. Waters J, Larkum M, Sakmann B, Helmchen F. Supralinear Ca2+ influx into dendritic tufts of layer 2/3 neocortical pyramidal neurons in vitro and in vivo. Journal of Neuroscience. 2003;23(24):8558-67.
62. Major G, Polsky A, Denk W, Schiller J, Tank DW. Spatiotemporally graded NMDA spike/plateau potentials in basal dendrites of neocortical pyramidal neurons. Journal of neurophysiology. 2008;99(5):2584-601.

1000 63. Harris JA, Mihalas S, Hirokawa KE, Whitesell JD, Choi H, Bernard A, et al. Hierarchical organization
1001 of cortical and thalamic connectivity. Nature. 2019;575(7781):195-202.
1002 64. Levelt CN, Hübener M. Critical-period plasticity in the visual cortex. Annual review of
1003 neuroscience. 2012;35:309-30.
1004 65. Bard JA, Zgombick J, Adham N, Vaysse P, Branchek TA, Weinshank RL. Cloning of a novel human
1005 serotonin receptor (5-HT7) positively linked to adenylate cyclase. Journal of Biological Chemistry.
1006 1993;268(31):23422-6.
1007 66. Karmarkar UR, Dan Y. Experience-dependent plasticity in adult visual cortex. Neuron.
1008 2006;52(4):577-85.
1009 67. Hensch TK, Bilimoria PM, editors. Re-opening windows: manipulating critical periods for brain
1010 development. Cerebrum: the Dana forum on brain science; 2012: Dana Foundation.
1011 68. Ogelman R, Gomez Wulschner LE, Hoelscher VM, Hwang I-W, Chang VN, Oh WC. Serotonin
1012 modulates excitatory synapse maturation in the developing prefrontal cortex. Nature Communications.
1013 2024;15(1):1368.
1014 69. Nolan MF, Malleret G, Dudman JT, Buhl DL, Santoro B, Gibbs E, et al. A behavioral role for dendritic
1015 integration: HCN1 channels constrain spatial memory and plasticity at inputs to distal dendrites of CA1
1016 pyramidal neurons. Cell. 2004;119(5):719-32.
1017 70. Wu J, El-Hassar L, Datta D, Thomas M, Zhang Y, Jenkins DP, et al. Interaction Between HCN and
1018 Slack Channels Regulates mPFC Pyramidal Cell Excitability and Working Memory. bioRxiv. 2023:2023.03.
1019 04.529157.
1020 71. Yu L, Tasaki S, Schneider JA, Arfanakis K, Duong DM, Wingo AP, et al. Cortical proteins associated
1021 with cognitive resilience in community-dwelling older persons. JAMA psychiatry. 2020;77(11):1172-80.
1022 72. Ramírez D, Zúñiga R, Concha G, Zúñiga L. HCN channels: new therapeutic targets for pain
1023 treatment. Molecules. 2018;23(9):2094.
1024 73. Ku SM, Han M-H. HCN channel targets for novel antidepressant treatment. Neurotherapeutics.
1025 2017;14(3):698-715.
1026 74. Kim CS, Johnston D. A possible link between HCN channels and depression. Chronic Stress.
1027 2018;2:2470547018787781.
1028 75. Postea O, Biel M. Exploring HCN channels as novel drug targets. Nature reviews Drug discovery.
1029 2011;10(12):903-14.
1030 76. Lyman KA, Han Y, Chetkovich DM. Animal models suggest the TRIP8b-HCN interaction is a
1031 therapeutic target for major depressive disorder. Expert Opinion on Therapeutic Targets. 2017;21(3):235-
1032 7.
1033 77. Fukuyama K, Motomura E, Okada M. Therapeutic potential and limitation of serotonin type 7
1034 receptor modulation. International Journal of Molecular Sciences. 2023;24(3):2070.
1035 78. Ishibashi T, Horisawa T, Tokuda K, Ishiyama T, Ogasa M, Tagashira R, et al. Pharmacological profile
1036 of lurasidone, a novel antipsychotic agent with potent 5-hydroxytryptamine 7 (5-HT7) and 5-HT1A
1037 receptor activity. Journal of Pharmacology and Experimental Therapeutics. 2010;334(1):171-81.
1038 79. Shimizu M, Mi X, Toyoda F, Kojima A, Ding W-G, Fukushima Y, et al. Propofol, an Anesthetic Agent,
1039 Inhibits HCN Channels through the Allosteric Modulation of the cAMP-Dependent Gating Mechanism.
1040 Biomolecules. 2022;12(4):570.
1041 80. Chen X, Shu S, Kennedy DP, Willcox SC, Bayliss DA. Subunit-specific effects of isoflurane on
1042 neuronal I h in HCN1 knockout mice. Journal of neurophysiology. 2009;101(1):129-40.
1043 81. Taylor AL. What we talk about when we talk about capacitance measured with the voltage-clamp
1044 step method. Journal of computational neuroscience. 2012;32(1):167-75.
1045 82. Desai NS, Gray R, Johnston D. A dynamic clamp on every rig. eneuro. 2017;4(5).
1046 83. Oláh VJ, Tarcsay G, Brunner J. Small size of recorded neuronal structures confines the accuracy in
1047 direct axonal voltage measurements. Eneuro. 2021;8(4).

1048 84. Testa-Silva G, Rosier M, Honnuraiah S, Guzulaitis R, Megias AM, French C, et al. High synaptic
1049 threshold for dendritic nmda spike generation in human layer 2/3 pyramidal neurons. Cell reports.
1050 2022;41(11).

1051